THE CARNEGIE-IRVINE GALAXY SURVEY. II. ISOPHOTAL ANALYSIS

Zhao-Yu Li[1,2], Luis C. Ho[2], Aaron J. Barth[3], and Chien Y. Peng[4]

To appear in The Astrophysical Journal Supplement.

ABSTRACT

The Carnegie-Irvine Galaxy Survey (CGS) is a comprehensive investigation of the physical properties of a complete, representative sample of 605 bright ($B_T \leq 12.9$ mag) galaxies in the southern hemisphere. This contribution describes the isophotal analysis of the broad-band (*BVRI*) optical imaging component of the project. We pay close attention to sky subtraction, which is particularly challenging for some of the large galaxies in our sample. Extensive cross-checks with internal and external data confirm that our calibration and sky subtraction techniques are robust with respect to the quoted measurement uncertainties. We present a uniform catalog of one-dimensional radial profiles of surface brightness and geometric parameters, as well as integrated colors and color gradients. Composite profiles highlight the tremendous diversity of brightness distributions found in disk galaxies and their dependence on Hubble type. A significant fraction of S0 and spiral galaxies exhibit non-exponential profiles in their outer regions. We perform Fourier decomposition of the isophotes to quantify nonaxisymmetric deviations in the light distribution. We use the geometric parameters, in conjunction with the amplitude and phase of the $m = 2$ Fourier mode, to identify bars and quantify their size and strength. Spiral arm strengths are characterized using the $m = 2$ Fourier profiles and structure maps. Finally, we utilize the information encoded in the $m = 1$ Fourier profiles to measure disk lopsidedness. The databases assembled here and in Paper I (Ho et al. 2011) lay the foundation for forthcoming scientific applications of CGS.

Subject headings: atlases — galaxies: fundamental parameters — galaxies: general — galaxies: photometry — galaxies: structure — surveys

1. INTRODUCTION

This paper, the second in a series, presents the isophotal analysis for the optical images of the Carnegie-Irvine Galaxy Survey (CGS), a detailed study of a statistically complete sample of nearby, bright galaxies in the southern sky (Ho et al. 2011, hereinafter Paper I). The immediate aim of this paper is to reduce our extensive set of images to a uniform database of one-dimensional (1-D) radial profiles of surface brightness and geometric parameters, on which much of our subsequent scientific analysis will depend. Although we intend to apply more sophisticated methods of analysis to the images (Peng et al. 2010; S. Huang et al., in preparation), the 1-D analysis already contains a wealth of useful information that can be exploited for science. Moreover, 1-D analysis has the virtue of simplicity. It can be efficiently applied to a large sample of objects, allowing a quick overview of the global properties of the survey.

The brightness profiles of galaxies have long helped to guide our understanding of their physical nature. Despite the visual complexity of their images, the 1-D radial brightness profiles of galaxies in the nearby Universe actually show a surprising degree of order. De Vaucouleurs (1948) first noticed that the light distributions of elliptical galaxies generally follow a $r^{1/4}$ profile, which has been interpreted as a signature of dissipationless formation processes (van Albada 1982; Katz 1991). Later studies, beginning with Caon et al. (1993), increasingly recognized that many ellipticals, in fact, do not strictly follow the $r^{1/4}$ law, but instead are better described by the more general $r^{1/n}$ function of Sérsic (1968), of which de Vaucouleur's law is a special case ($n = 4$). Indeed, the Sérsic function has since

been generally adopted as the standard formula for fitting the brightness profiles of ellipticals (e.g., Graham et al. 1996; Trujillo et al. 2001; Kormendy et al. 2009). Our modern view of bulges has also grown steadily more complex over time. Once thought to be mini-ellipticals with $r^{1/4}$ profiles, bulges, too, are now known to be better described by a Sérsic $r^{1/n}$ function (Andredakis & Sanders 1994; Andredakis et al. 1995; de Jong 1996; Courteau et al. 1996; MacArthur et al. 2003). The Sérsic indices of bulges have a broad distribution of observed values, from $n < 1$ to $n > 4$ (e.g., MacArthur et al. 2003; Fisher & Drory 2008; Gadotti 2008), and it is argued that they reflect different formation physics. Spheroids with $n \lesssim 2$ are regarded as pseudobulges (Fisher & Drory 2008), which formed through internal, secular processes, while those with $n \gtrsim 2$ are classical bulges, which, like the ellipticals, were assembled more rapidly, most likely with the assistance of mergers (Kormendy & Kennicutt 2004).

The brightness profiles of the disks of S0 and spiral galaxies have been traditionally described by a single exponential function (de Vaucouleurs 1959; Freeman 1970), which arises as a natural consequence of viscous transport in a disk (Yoshii & Sommer-Larsen 1989; Zhang & Wyse 2000; Ferguson & Clarke 2001; Slyz et al. 2002), perhaps mediated by star formation and feedback processes (Robertson et al. 2004; Governato et al. 2007). In actuality, very few disks are so simple. Many possess breaks and inflections in their outer radial profile (van der Kruit 1979; van der Kruit & Searle 1981; Matthews & Gallagher 1997; Pohlen et al. 2000; de Grijs et al. 2001; Erwin 2005; Erwin et al. 2005; Pohlen & Trujillo 2006). No general consensus yet exists as to their cause, but they offer important

[1] Department of Astronomy, School of Physics, Peking University, Beijing 100871, China

[2] The Observatories of the Carnegie Institution for Science, 813 Santa Barbara Street, Pasadena, CA 91101

[3] Department of Physics and Astronomy, 4129 Frederick Reines Hall, University of California, Irvine, CA 92697-4575

[4] NRC Herzberg Institute of Astrophysics, 5071 West Saanich Road, Victoria, British Columbia, Canada V9E 2E7

clues to a host of physical processes pertinent to galaxy formation (van der Kruit & Freeman 2011).

Apart from intensity profiles, isophotal analysis of galaxy images yields other useful diagnostics. The radial variation of the ellipticity and position angle, for example, provides an efficient means to identify bars and to quantify their length and strength (e.g., Laine et al. 2002; Erwin 2005; Menéndez-Delmestre et al. 2007). Fourier decomposition of the isophotes provides yet another method to probe nonaxisymmetric perturbations in the light distribution. The relative amplitude of the $m = 2$ mode, in combination with its phase angle, has been shown to be effective in isolating bars (Elmegreen & Elmegreen 1985; Buta 1986; Ohta et al. 1990) and spirals (Elmegreen et al. 1989; Rix & Zaritsky 1995; Odewahn et al. 2002). Both of these features are common constituents in disk galaxies, and both are thought to play a dynamical role in facilitating angular momentum transport and driving secular evolution. Likewise, a significant fraction of disk galaxies exhibits global lopsidedness in their stellar light distribution (Rix & Zaritsky 1995; Zaritsky & Rix 1997; Bournaud et al. 2005; Reichard et al. 2008), whose main culprit remains in dispute (Jog & Combes 2008). As shown by Rix & Zaritsky (1995), this type of nonaxisymmetric perturbation is again conveniently revealed through Fourier analysis of the isophotes, in this case through the $m = 1$ mode.

This paper is organized as follows. Section 2 gives a brief overview of the CGS sample, the observations, and some basic characteristics of the images. Section 3 describes our method of sky subtraction. The procedural details of isophotal analysis are presented in Section 4, including our method for extracting geometric parameters, surface brightness profiles, and Fourier components. We generate composite light distributions (Section 5) to identify statistical trends in disk profiles, and assemble integrated colors and color gradients (Section 6). The products from the isophotal and Fourier analysis are used to quantify the strengths of bars (Section 7), spiral arms (Section 8), and lopsidedness (Section 9). Section 10 assesses the reliability of our measurements using internal and external tests. Section 11 gives a brief summary and an outline of future plans. The database of isophotal parameters is described in the Appendix.

2. SAMPLE PROPERTIES

The CGS covers a statistically complete sample of 605 bright, nearby galaxies of all morphological types in the southern hemisphere, with B-band total magnitude $B_T \leq 12.9$ and $\delta < 0°$. These very general selection criteria enable us to probe galaxies with a broad range of physical properties and morphologies. The primary parent sample[5] comprises 17% ellipticals, 18% S0 and S0/a, 64% spirals, and 1% irregulars. The bulk of the sample is relatively nearby (median $D_L = 24.9$ Mpc), luminous (median $M_{B_T} = -20.2$ mag), and well resolved. The typical seeing of CGS is $\sim 1''$, and the sample has a median isophotal angular diameter of $D_{25} = 3'.3$ at a surface brightness level of $\mu_B = 25$ mag arcsec^{-2}.

Paper I describes the observing strategy, data reductions, and photometric calibration of the optical imaging component of the project. We only repeat a few essential details here. The broad-band $BVRI$ images have a field-of-view of $8'.9 \times 8'.9$ and a pixel scale of $0''.259$, which is well matched to the good seeing typically achieved with the du Pont 2.5-m telescope at Las Campanas Observatory. The median seeing of the survey, as determined from over 6000 science images, is $1''.17$, $1''.11$, $1''.01$, and $0''.96$ in the B, V, R, and I band, respectively. A little more than half of the galaxies were observed under photometric conditions, with median photometric errors of 0.08, 0.04, 0.03, and 0.04 mag for the B, V, R and I filters, respectively. We devised a calibration strategy to establish an approximate photometric zeropoint for the nonphotometric observations, for which the corresponding photometric errors are 0.21, 0.11, 0.10, and 0.09 mag. After correcting for large-scale gradients in the background, the flatness of the final images is about 0.6%, and the typical depth of the surface brightness, defined as 1σ above the background, has a median value of $\mu \approx 27.5, 26.9, 26.4,$ and 25.3 mag arcsec^{-2} in the $B, V, R,$ and I bands, respectively.

We derived a number of data products from the reduced, calibrated images. These include red-green-blue color composites generated from the B, V, and I bands, images cleaned of foreground stars and background galaxies, a stacked image from a weighted combination of the four filters optimized to enhance regions of low surface brightness, structure maps designed to accentuate high-spatial frequency features, and color index maps from different combinations of the filters.

3. SKY DETERMINATION

Sky determination is a crucial, fundamental step in the data analysis. Many of the basic galaxy parameters we are interested in measuring (magnitudes, colors, characteristic size and brightness level, etc.) are predicated on having the sky level properly subtracted. Importantly, under-subtraction or over-subtraction of the sky value can introduce spurious curvature into the brightness profile, especially in the faint, outer regions of the galaxy (e.g., Erwin et al. 2008). MacArthur et al. (2003) studied the influence of the sky value on the bulge and disk parameters for a sample of spirals, and concluded that the disk, but to a lesser extent even the bulge, parameters are sensitive to the sky value.

There are a variety of ways to measure the sky value of a CCD image. Science data such as ours, however, wherein an extended object fills a substantial portion of the chip, pose unique challenges. This is especially so because the background of our images is not always entirely uniform (Paper I). We adopt a two-step approach. As in Noordermeer & van der Hulst (2007), we generate the isophotal intensity radial profile of the galaxy to the edge of the field to determine the radius beyond which the sky background dominates the signal. As illustrated in Figure 1, the transition from the galaxy's outer boundary to the sky-dominated region manifests itself as flattening of the radial profile, beyond which it oscillates about a constant intensity level. To be specific, we define the outer radius to be the first data point where the measured isophotal intensity rises instead of decreases monotonically. Typically the outer radius is large enough to avoid the spiral arms or other features that may cause a real rise in the outer brightness profile. In the standard procedure of Noordermeer & van der Hulst (2007), the average value of this isophotal intensity outside the outer radius and the associated standard deviation gives estimates of the sky level and its uncertainty. However, this technique is reliable only if the background is uniform and well measured (Erwin et al. 2008). The field-of-view of our images is typically only a factor of ~ 2 larger than the galaxies, generally too marginal to provide enough data points in the sky-dominated region to yield a statistically robust measurement of the background and

---

[5]As described in Paper I, we observed an additional 11 galaxies that do not formally meet the selection criteria of CGS. We still analyze them here but will not use their results to draw statistical inferences on the sample.
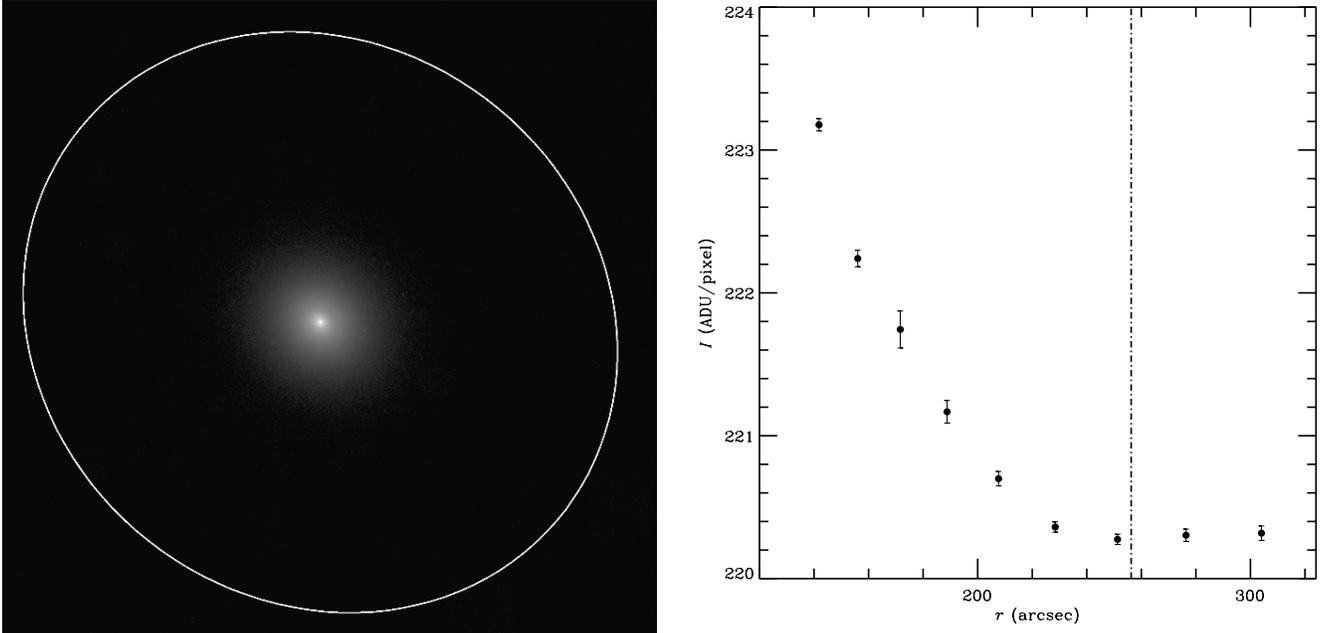
FIG. 1.— Illustration of how we determine the sky radius for the *B*-band image of NGC 1400. (*Left*) Star-cleaned image, showing the full field-of-view of $8'.9 \times 8'.9$. (*Right*) Radial profile of the isophotal intensity, in units of ADU pix^{-1}. The vertical dash-dotted line marks the radius where the isophotal intensities start to oscillate rather than continue to decrease; this radius, designated by the keyword SKY_RAD in the image header, denotes the region outside of which the sky dominates. The corresponding isophotal ellipse is overplotted on the left-hand panel.
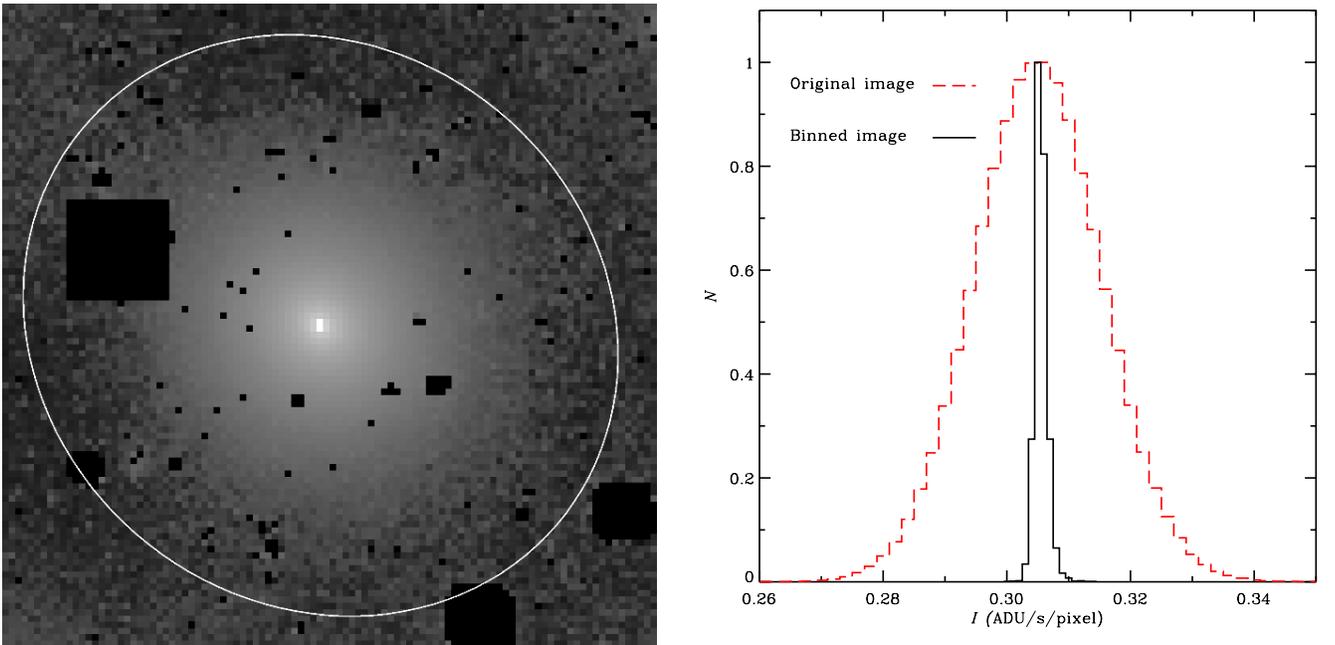
FIG. 2.— (*Left*) *B*-band image of NGC 1400, binned by 20×20, with the ellipse in Figure 1 overplotted. We show the full field-of-view of $8'.9 \times 8'.9$. The sky value and its uncertainty are simply the mean and standard deviation of the pixel values outside of this ellipse, after excluding the masked objects, which are shown as black regions. (*Right*) Normalized histograms of the background pixels of the original and the binned images; their peak positions are 0.3060 ± 0.0102 and 0.3059 ± 0.0011 ADU s^{-1} pix^{-1}, respectively.

its error. The situation is further exacerbated by the occasional presence of residual large-scale non-uniformities in the background. In view of these complications, we use Noordermeer & van der Hulst's method only to determine the radius of the sky-dominated region (Figure 1), which we record in the image header under the keyword SKY_RAD.

To estimate the actual sky value and its associated error, we follow a method similar to that used by Erwin et al. (2008). We first smooth the original 2042×2042 pixel image by binning it down to a 102×102 pixel image. This highlights underlying large-scale, systematic fluctuations in the background, which is the main factor that ultimately limits the accuracy with which we can determine the sky level, and hence the final sensitivity of the surface brightness of our images. The value of each binned pixel is the mean value of all the pixels inside a 20×20 pixel box, after excluding field stars and background galaxies
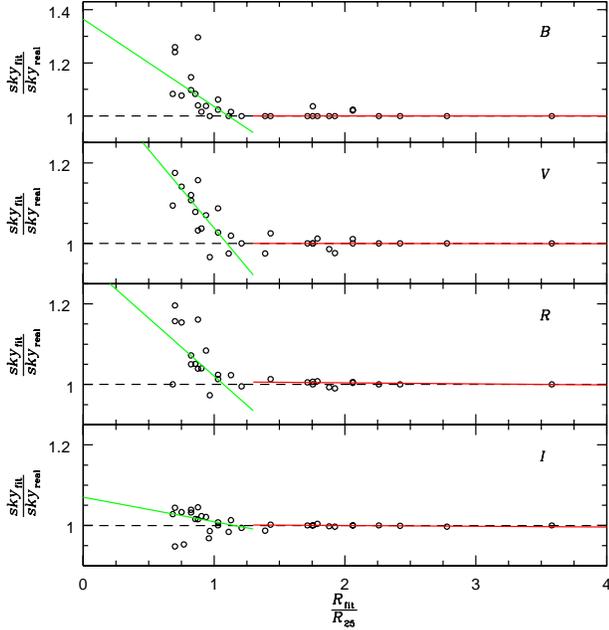
FIG. 3.— Empirical relationship between sky_{fit}/sky_{real} and R_{fit}/R_{25}, for each of the four filters. For $R_{fit}/R_{25} \gtrsim 1.3$, $sky_{fit} \approx sky_{real}$ as indicated by the best-fitted red solid lines with slopes close to 0, but when $R_{fit}/R_{25} \lesssim 1.3$, sky_{fit} is systematically larger than sky_{real}. The green solid lines represent the best-fit linear relations given by Equations 1–4.

identified in the image's object mask (Paper I). The background pixels, then, are defined to be all the pixels in the binned image outside of the isophotal ellipse marked by SKY_RAD. The sky level is simply the mean of the background pixel values, and its uncertainty is the standard deviation of the pixel flux distribution; these values are stored in the image header under the keywords SKY_VAL and SKY_ERR. (The standard deviation of the mean, useful for other applications, is stored separately under the keyword SKY_SIG.) We have opted to compute the mean of the pixel flux distribution, rather than its median or mode, but in practice this makes little difference (they generally agree to ~0.1%) because the shape of the distribution is highly symmetrical. This reflects the robustness of our estimate of the sky-dominated region and the effectiveness of our object masks in rejecting faint halos around foreground stars and background galaxies.

We have tested the effect of choosing different scales for the smoothing, varying the binning box sizes from 5 to 50 pixels. While the average sky value remains stable, the width of the pixel distribution decreases with increasing smoothing length, leveling off to a near-constant value for box sizes $\gtrsim$20 pixels (~5″). We interpret this to represent the typical scale of large-scale systematic fluctuations in the sky background. We choose a box size of 20×20 pixel as a reasonable compromise in order to retain a statistically significant number of data points to compute their average and standard deviation.

Figure 2 illustrates our method of sky estimation, using a B-band image of NGC 1400. The image has been binned 20×20, and the foreground stars and background galaxies have been masked out. The sky value is the mean of pixel values outside of the ellipse, after excluding the masked objects, and the error is simply the standard deviation of the sky pixels in the binned image. The right-hand panel shows normalized histograms of the sky pixels of the original and binned image. Clearly they peak at nearly identical locations (the peaks of the two his-

tograms differ by 0.0001 ADU s^{-1} pix^{-1}), but the distribution for the binned image is narrower than that of the original image by a factor of 10.

The above-described strategy for sky determination can only be applied to galaxies with angular diameters $D_{25} \lesssim 5'$–$6'$. For the ~15% of the sample more extended than this, it is difficult to impossible to determine the radius of the sky-dominated region and obtain robust statistics for the sky pixels, and we must resort to a more indirect approach. The signal in the outer regions of the CCD frame consists of galaxy light plus a constant sky background. Assuming that the galaxy component can be modeled by a single Sérsic function, we can fit the observed light profile to solve for the underlying sky value. We perform the fitting on the 1-D surface brightness profile (Section 4), after excluding the central regions of the galaxy and other features such as the bulge, the bar, or strong spiral arms, if present. Simple experimentation shows that the best-fit sky value depends on the fitting radius relative to the size of the galaxy. Clearly, if the fitting radius is large compared to the outer edge of the galaxy, the sky will be well determined; however, if the fitting radius lies substantially interior to the main body of the galaxy, the inferred sky value will depend critically on how well the Sérsic model represents the intrinsic light profile of the galaxy.

We devise an empirical correction, as follows. We select several galaxies that (1) have relatively simple structures, (2) are small compared to the CCD's field-of-view, and (3) have well-determined sky values. Then, we fit their surface brightness profiles with different fitting radii (R_{fit}), to mimic the actual situation in galaxies that are too angularly extended to have a reliable sky determination. The resulting fitted sky value, sky_{fit}, is then compared with the independently known, correct value sky_{real}. Figure 3 shows sky_{fit}/sky_{real} versus R_{fit}/R_{25}, where $R_{25} = 0.5 D_{25}$. We can see that $sky_{fit}/sky_{real} \approx 1$ when $R_{fit}/R_{25} \gtrsim 1.3$. When $R_{fit}/R_{25} \leq 1.3$, sky_{fit} overestimates sky_{real}, but it does so systematically, in such a way that we can apply an approximate empirical correction to recover the true sky value. The best-fitting linear relations (and their associated RMS scatter), are:

- B band
$$\frac{sky_{fit}}{sky_{real}} = 1.364 - 0.327 \times \frac{R_{fit}}{R_{25}}, \qquad \sigma = 0.05, \qquad (1)$$

- V band
$$\frac{sky_{fit}}{sky_{real}} = 1.427 - 0.389 \times \frac{R_{fit}}{R_{25}}, \qquad \sigma = 0.033, \qquad (2)$$

- R band
$$\frac{sky_{fit}}{sky_{real}} = 1.309 - 0.287 \times \frac{R_{fit}}{R_{25}}, \qquad \sigma = 0.042, \qquad (3)$$

- I band
$$\frac{sky_{fit}}{sky_{real}} = 1.070 - 0.060 \times \frac{R_{fit}}{R_{25}}, \qquad \sigma = 0.020. \qquad (4)$$

The best-fit sky value, sky_{fit}, and its associated statistical error, σ_{fit}, are recorded under the header keywords SKY_VAL and SKY_ERR with the comment "fitted sky value." If the above empirical correction to sky_{fit} is necessary, we fold the scatter of the correction relation into the error budget.

4. ISOPHOTAL ANALYSIS

4.1. *Geometric Parameters and Surface Brightness Profile*

The IRAF[6] task *ellipse* is commonly used to measure the surface brightness profiles of galaxies (e.g., Silva & Elston 1994; Milvang-Jensen & Jøgensen 1999; Laine et al. 2002; Jogee et al. 2004; Aguerri et al. 2005; Marinova & Jogee 2007; Noordermeer & van der Hulst 2007; Barazza et al. 2008). Following the iterative method of Jedrzejewski (1987), we fit the isophotes of the galaxy with a set of ellipses. This is motivated by the fact that the isophotes of most galaxies, especially early-type systems such as ellipticals and lenticulars, are quite close to ellipses[7]. In our implementation, the ellipses are sampled along the semi-major axis of the galaxy in logarithmic intervals, starting from $r \approx 0.''3$ and increasing the radius of each successive ellipse by a factor of 1.1. After reaching the outermost ellipse, the fitting reverses direction and moves toward the galaxy center from $r \approx 0.''3$, with each subsequent radius decreasing by a factor of 1.1.

As in Noordermeer & van der Hulst (2007), we determine the isophotal geometric parameters of the galaxy in two steps. In the first step, we estimate the center of the galaxy. Ellipses are fitted to the *I*-band image with the center, position angle (PA), and ellipticity (*e*) set as free parameters. We use the *I*-band image as the fiducial reference because of its relative insensitivity to dust extinction and young stars, and because it generally has the best seeing. The center of the galaxy is the average central position of the ellipses inside $\sim 5''$–$7''$. In images of regular galaxies the center of the best-fit ellipses often converge to a well-defined value, with RMS $\approx 0.''015$. However, in galaxies with dusty nuclear regions, the best-fitting central isophotes may give a poor measure of the true center. In such cases, a better estimate of the true center comes from isophotes at intermediate radii, $\sim 10''$–$30''$, far enough to be undisturbed by central dust but yet sufficiently close to the nucleus to give a faithful measure of its position. The typical uncertainty of the central positions estimated in this way is $\sim 0.''02$.

Next, we fix the center just determined and run *ellipse* again, while still setting *e* and PA free. Our goal is to determine the characteristic *e* and PA of the galaxy based on its best-fit isophotes. Typically we take the average value of these parameters in the outer regions of the galaxy, where the intensity is about $1\,\sigma$ above the sky, as their characteristic values and use their standard deviations over that region as the uncertainties. These parameters usually converge to a constant value within that region, with variations of ~ 0.04 for *e* and $\sim 2°$ for PA. However, the intrinsic geometric parameters of some galaxies can be distorted by mergers or interactions, causing *e* and PA to diverge at large radii. In these cases we simply estimate their values manually from the visually best-fitting isophotes near the edge of the galaxy. The *B*, *V*, *R*, and *I* images have their center, *e*, and PA values determined independently, and they are stored in their corresponding image headers.

During this second step, we also record the deviations of the isophotes from perfect ellipses, which, as described in Jedrzejewski (1987), are parameterized by the third (A_3, B_3) and fourth (A_4, B_4) harmonics of the intensity distribution. The A_3 and B_3 parameters give "egg-shaped" or "heart-shaped" isophotes (Carter 1978; Jedrzejewski 1987). Peletier et al. (1990) point out that A_3 and B_3 appear to be sensitive diagnos-

tics of dust features in elliptical galaxies. The most interesting parameter among them is B_4: if it is positive, the underlying isophote is disky with respect to a perfect ellipse; a negative B_4 corresponds to a boxy isophote. Figure 1 of Peletier et al. (1990) gives examples of the different isophotal shapes for different values of B_3, A_4, and B_4.

We run *ellipse* for a third and final time to extract the average intensity of the isophotes, fixing the geometric parameters to the values determined above (e.g., Pohlen & Trujillo 2006; Noordermeer & van der Hulst 2007). For this step, we do not allow the geometric parameters to vary in order to reduce the influence of bars and other nonaxisymmetric features on the average intensity profile, as well as to reach convergence in regions where the signal-to-noise ratio (S/N) is marginal (Erwin et al. 2008). For consistency, we apply this isophote measurement to all the galaxies in our sample. For the lopsided galaxies, we also experimented with allowing the isophotal centers to be left as free parameters. We find that the typical difference in the brightness profile, compared with the fits based on fixed isophotal centers, is ~ 0.2 mag arcsec^{-2}. Moreover, our tests show that the relative amplitudes of the Fourier terms (§4.2) decrease significantly when the isophotal centers are allowed to be free, due to the fact that the free-fitting ellipses can better trace the distorted disk in the outer part of the galaxy to produce very small fluctuations along each isophote. This will make the Fourier analysis less effective for detecting and quantifying the properties of bars or lopsided structures.

After subtracting the sky background from the image, the surface brightness is calculated from

$$\mu = -2.5 \log \left(\frac{I_{\mathrm{iso}}}{t_{\mathrm{exp}} \times A} \right) + zpt, \tag{5}$$

where I_{iso} is the isophotal intensity after subtracting the sky, t_{exp} is the exposure time of the image in units of seconds, A is the pixel area in units of arcsec^2, and zpt is the photometric zeropoint of the image in units of magnitudes. We calculate the surface brightness only from those isophotes whose intensities are larger than $I_{\mathrm{sky}} + \sigma_{\mathrm{sky}}$. We propagate the errors on I_{iso} into errors on μ in magnitude units. The surface brightness profiles in the *B*, *V*, and *R* bands are constrained to have the same geometric parameters as determined in the *I* band.

To construct 1-D color profiles, we blur all the images to a common seeing. This is done by convolving the image having the better seeing with a two-dimensional (2-D) Gaussian function whose full width at half maximum (FWHM) is the quadrature difference between the two seeing values. The measured isophotal ellipses of the unblurred *I*-band image are used to directly calculate the isophotal intensity of the blurred images in all the filters. Color profiles follow from straightforward differencing of one band from another.

4.2. *Fourier Analysis*

We study the harmonic components of the intensity distribution of the isophotes. In our work, we decompose the intensity distribution along each ellipse into a Fourier series of the form

---

[6]IRAF is distributed by the National Optical Astronomy Observatory, which is operated by the Association of Universities for Research in Astronomy, Inc., under cooperative agreement with the National Science Foundation.

[7]An important exception are edge-on galaxies, which are not well suited to ellipse fits. As the bulge and disk components have different profiles and ellipticities, their relative contributions change with radius and azimuth (i.e. along major or minor axes). A dust lane, if present, also can strongly affect the averaged isophotal intensity. For edge-on galaxies it is preferable to extract the isophotal intensities along cuts in the major and minor axis directions (e.g., de Grijs 1998; Fry et al. 1999; Wu et al. 2002).
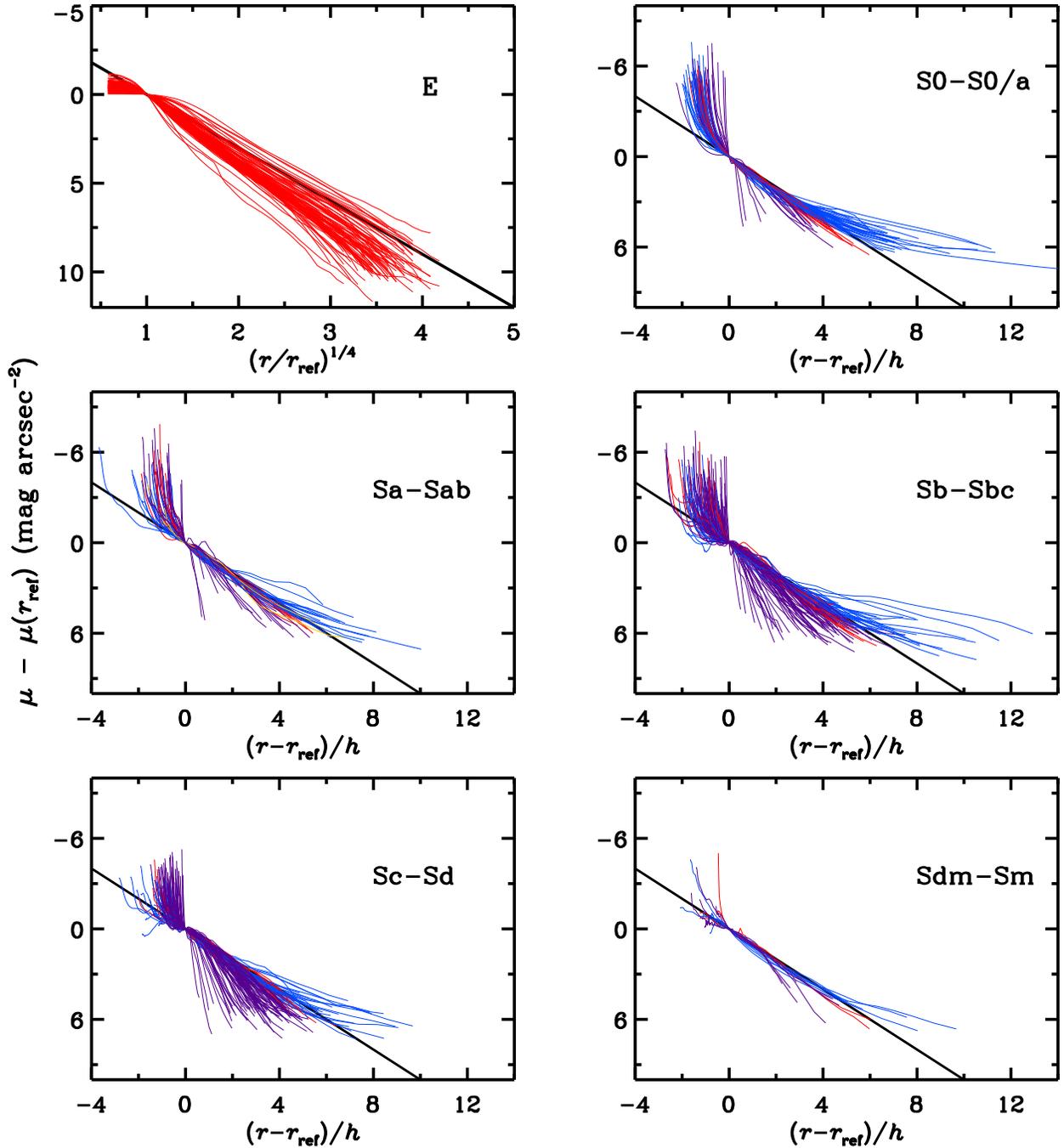
FIG. 4.— B-band composite profiles of our sample, divided by morphological type. The elliptical galaxies are normalized at a reference radius of $r_{ref} = R_{20}$, and the profiles are plotted versus $(r/r_{ref})^{1/4}$. The thick black line corresponds to a de Vaucouleurs $r^{1/4}$ law. The profiles for the disk galaxies are scaled according to the scale length h of the disk outside r_{ref}. Profiles of Type I, II, and III are marked in red, purple, and blue, respectively. The thick black line corresponds to a pure exponential function.

$$I(\theta) = I_0 + \sum_{j=1}^{\infty} I_j \cos j(\theta + \phi_j), \qquad (6)$$

where I is the intensity (in units of ADU s^{-1} pix^{-1}) on the ellipse in the direction θ, I_0 is the average intensity of the ellipse, I_j measures the strength of the jth mode in the series, and ϕ_j is the corresponding phase angle of that mode. The angle θ is defined to be 0° along the positive y-axis and increases coun-

terclockwise; $\phi_j = 0°$ along the positive y-axis and increases clockwise. A high S/N is required to derive a statistically significant measurement of the high-order Fourier terms (Noordermeer & van der Hulst 2007); thus, we only perform this decomposition inside the radius where the average intensity of the isophote is $3\sigma_{sky}$ larger than the determined sky value. The relative amplitude of the $m = 1$ (I_1/I_0) and $m = 2$ (I_2/I_0) mode will be especially useful in our analysis, as they reflect the lopsidedness of the galaxy (Rix & Zaritsky 1995) and the strength of
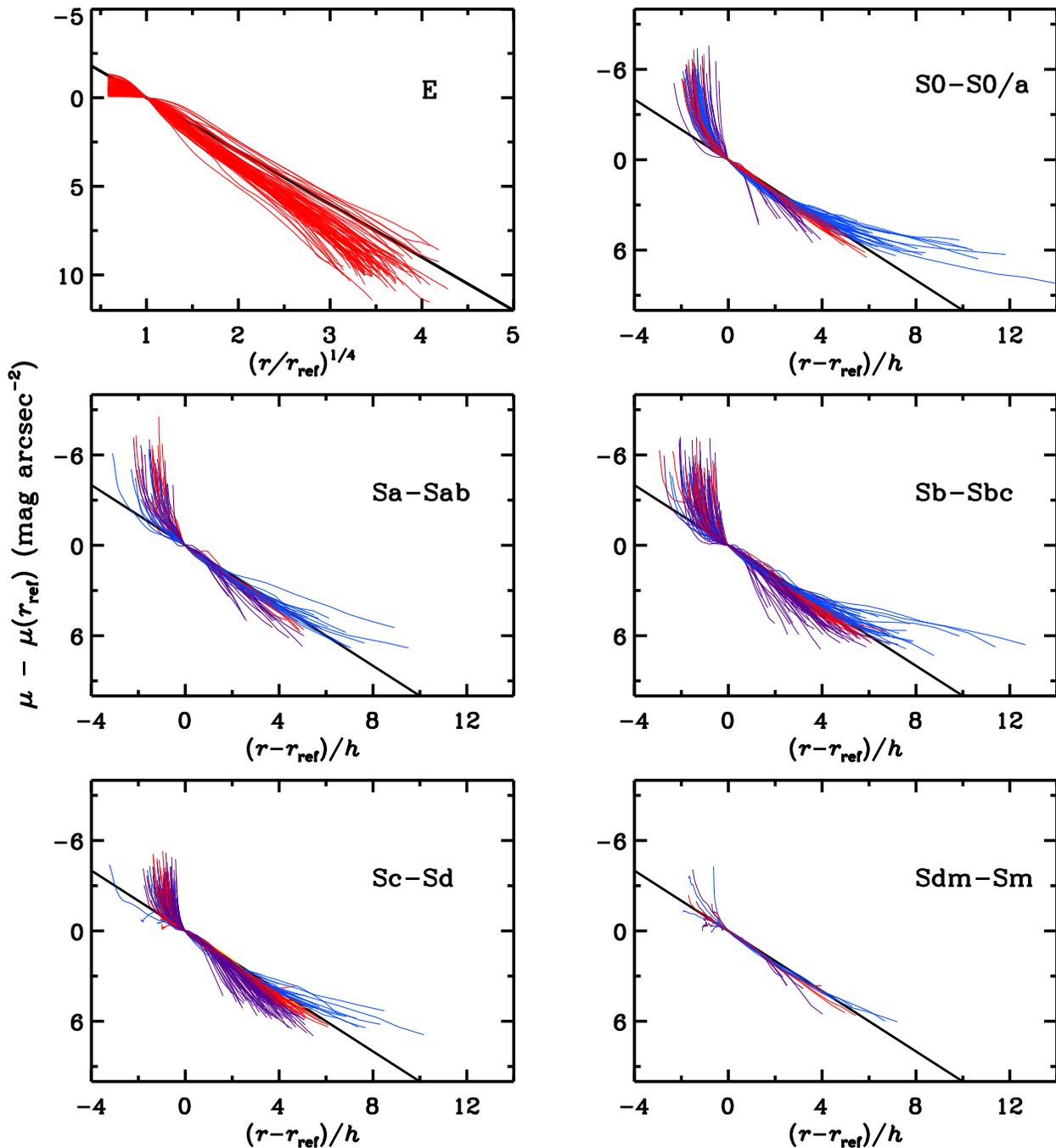
FIG. 5.— *I*-band composite profiles of our sample. See Figure 4 for details.

the bar or spiral arms (Buta 1986), respectively.

Buta (1986) performed a Fourier analysis to study the azimuthal variations of the light distribution of NGC 1433, which is also included in the CGS sample. We found good agreement between Buta's values of the relative amplitudes of the $m = 1$ and 2 modes and those calculated by us. This helps to confirm the robustness of our method.

4.3. *Database of 1-D Profiles*

The full database of isophotal parameters for the 605 galaxies in CGS (including the 11 extras not for-

mally part of the survey) is given in the Appendix, as Figures A1–A616, as well as on the project website http://cgs.obs.carnegiescience.edu.

5. COMPOSITE PROFILES

Composite profiles can help to highlight characteristic statistical trends, as well as to isolate interesting outliers, in a class of objects. We normalize the surface brightness profiles to a common reference radius. For the elliptical galaxies in our sample, we set r_{ref} to R_{20}, the radius wherein 20% of the total flux is enclosed, and plot the profiles as a function of $(r/r_{ref})^{1/4}$. In this reference frame, a classical de Vaucouleurs $r^{1/4}$ profile traces a

TABLE 1: FREQUENCY OF PROFILE TYPES FOR THE DISK GALAXIES

Hubble Type (1)	T (2)	Filter (3)	Number (4)	Type I (5)	Type II (6)	Type III (7)	Other (8)
S0–S0/a	$-3 \leq T < 0.5$	B	75	16.0%	26.7%	57.3%	0.0%
		V	78	20.5%	26.9%	52.6%	0.0%
		R	75	24.0%	24.0%	52.0%	0.0%
		I	81	30.9%	19.8%	49.3%	0.0%
Sa–Sab	$0.5 \leq T < 2.5$	B	51	17.6%	39.2%	39.2%	4.0%
		V	52	15.4%	40.4%	40.4%	3.8%
		R	53	18.9%	37.7%	41.5%	1.9%
		I	52	30.8%	34.6%	34.6%	0.0%
Sb–Sbc	$2.5 \leq T < 4.5$	B	132	12.1%	63.6%	24.3%	0.0%
		V	134	20.1%	53.7%	24.6%	1.6%
		R	135	22.2%	49.6%	26.7%	1.5%
		I	135	27.4%	45.2%	27.4%	0.0%
Sc–Sd	$4.5 \leq T < 7.5$	B	137	7.3%	72.3%	19.7%	0.7%
		V	138	10.1%	71.0%	18.1%	0.8%
		R	137	13.1%	67.2%	18.2%	1.5%
		I	137	27.7%	56.2%	14.6%	1.5%
Sdm–Sm	$7.5 \leq T < 9.5$	B	17	23.5%	35.3%	41.2%	0.0%
		V	17	23.5%	35.3%	41.2%	0.0%
		R	16	31.3%	37.5%	31.2%	0.0%
		I	17	29.4%	29.4%	41.2%	0.0%

NOTE.— Col. (1) Hubble type. Col. (2) Morphological type index. Col. (3) Filter. Col. (4) Number of objects. Cols. (5)–(7) Fraction with profiles of Type I, II, and III, respectively. Col. (8) Other complicated profiles.

straight line. Figure 4 (top left panel) illustrates the now-known fact that not all ellipticals obey the $r^{1/4}$ law, but rather are better described by a more general Sérsic function with $r^{1/n}$.

For the disk (S0 and spirals) galaxies, we set $r_{\rm ref}$ to be roughly the boundary between the bulge and disk, and we plot the brightness profiles as a function of $(r - r_{\rm ref})/h$, where h is the scale length of the disk, as determined by fitting an exponential function to the profile outside of $r_{\rm ref}$. This choice of coordinates helps to reveal possible deviations of the disks from a canonical exponential profile ($n = 1$), which appears as a straight line. It is apparent that the light distributions of the disk very rarely follow a pure exponential function (Figure 4), especially in their outer regions. Most show a downward turn compared to a single exponential, but not an insignificant number show an upward turn. This phenomenon is well-known (e.g., Phillipps et al. 1991; Erwin 2005; Erwin et al. 2005; Pohlen & Trujillo 2006). We code the three profile types with different colors, with Type I profiles (no break) in red, Type II profiles (downward break) in purple, and Type III profiles (upturn) in blue. The scatter among the normalized profiles is smaller in the redder bands, indicating that dust extinction and young stars have a greater effect on the profile shapes in the blue. Figure 5 shows the equivalent montage for the I band.

Table 1 tabulates the frequency of the different profiles for each bin of morphological type for the disk galaxies. Occasionally, there are some galaxies with complicated surface brightness profiles, which cannot be classified as any of the

three standard types listed above. The profiles for such objects are listed as "Other" in Table 1[8]. Type II and Type III profiles are common in our sample, and their fractions depend on the galaxy morphology. Type II profiles occur more frequently in late-type disk galaxies ($\sim 70\%$ among Sc–Sd spirals), whereas Type III profiles are preferentially found in more bulge-dominated, earlier-type systems, especially among the S0–S0/a class ($\sim 50\% - 60\%$). The fraction of galaxies with Type I profiles, on the other hand, seems to be roughly constant, at $\sim 20\%$, across all morphological types; the fraction increases systematically toward redder bandpasses, except for the Sdm–Sm galaxies, where the fraction seems to be roughly constant, although the number of objects is small. A detailed analysis of the different profile types and their dependence on other physical parameters will be presented in a separate paper.

6. COLOR INFORMATION

Table 2 presents integrated colors and color gradients for the sample, corrected for foreground Galactic extinction using values from Schlegel et al. (1998). We list $B - I$, $V - I$, and $R - I$, from which other color combinations can be readily derived; we use total magnitudes within the last reliable isophote (1 σ above the sky), as given in Table 4 of Paper I. For each of these color combinations, we also calculate two simple measures of the color gradient, after resampling the color profiles with 300 equally spaced data points in linear space, to overcome the heavily sampled points in the central region.

[8]Since the brightness profile in the outer regions of the galaxy depends sensitively on the accuracy of the sky subtraction, we exclude objects with unreliable sky determination. We also omit galaxies whose light distribution is severely adversely affected by very bright foreground stars, by excessively crowded field stars, or by an interacting neighbor. The excluded objects are flagged in Table 2. Note that a star that is bright and excluded in one filter may not be equally bright or rejected in another; therefore, the number of objects in a morphological bin is not the same among all the filters. We further omit the 11 extra galaxies that do not formally meet the CGS selection criteria.

TABLE 2: Integrated Colors and Color Gradients for the CGS Sample

Index	Name	$B-I$ (mag)	$V-I$ (mag)	$R-I$ (mag)	$\nabla(B-I)_{\rm in}$	$\nabla(B-I)_{\rm out}$	$\nabla(V-I)_{\rm in}$	$\nabla(V-I)_{\rm out}$	$\nabla(R-I)_{\rm in}$	$\nabla(R-I)_{\rm out}$	Notes
(1)	(2)	(3)	(4)	(5)	(6)	(7)	(8)	(9)	(10)	(11)	(12)
1	ESO 009-G010	1.83±0.06	1.22±0.05	0.68±0.05	−0.19±0.05	0.30±0.77	−0.08±0.04	0.01±0.72	0.00±0.04	0.11±0.73	
2	ESO 027-G001	1.31±0.30	0.90±0.21	0.52±0.19	−0.67±0.17	−0.19±0.73	−0.32±0.10	−0.07±0.72	−0.11±0.08	0.03±0.73	
3	ESO 027-G008	1.96±0.30	1.26±0.21	0.63±0.19	−0.41±0.08	0.80±0.66	−0.18±0.07	0.69±0.65	−0.07±0.07	0.61±0.61	extra $BVRI$[b]
4	ESO 056-G115	⋯	⋯	⋯	⋯	⋯	⋯	⋯	⋯	⋯	
5	ESO 060-G019	1.42±0.30	1.08±0.21	0.65±0.19	0.23±0.13	0.55±1.02	0.19±0.12	0.47±1.00	0.20±0.12	0.39±0.98	
6	ESO 091-G003	1.67±0.05	1.04±0.05	0.49±0.04	−0.12±0.07	−0.65±0.36	0.01±0.06	−0.25±0.34	0.08±0.05	0.00±0.34	extra $BVRI$[b,e]
7	ESO 097-G013	⋯	⋯	⋯	0.01±0.10	−1.10±1.10	0.07±0.09	−0.27±1.09	0.09±0.08	−0.39±1.04	I[a]
8	ESO 121-G006	1.97±0.14	1.42±0.09	0.82±0.08	−0.77±0.14	0.14±0.55	−0.40±0.12	0.38±0.51	−0.13±0.10	0.44±0.56	
9	ESO 121-G026	1.68±0.14	1.15±0.09	0.63±0.08	−0.52±0.08	−0.89±0.29	−0.19±0.05	−0.46±0.28	−0.06±0.04	−0.19±0.28	
10	ESO 136-G012	1.31±0.39	1.12±0.26	0.75±0.19	−0.30±0.25	0.06±2.00	−0.08±0.23	0.01±1.90	0.06±0.24	0.28±2.01	$BVRI$[b]

NOTE.— Col. (1) Numerical index. Col. (2) Galaxy name. Cols. (3)–(5) Integrated colors derived from the total magnitudes within the last reliable isophote (1 σ above the sky). Cols. (6)–(11) Color gradients of the galaxy interior and exterior to R_{50} measured in the I band (see Section 6). The units are Δmag per dex in radius. The colors and color gradients have been corrected for Galactic extinction. Col. (12) Notes: "extra" = object not formally part of the main sample; filters = image of that filter has problem, which is indicated by the table mark. *Table 2: Integrated Colors and Color Gradients for the CGS Sample is presented in its entirety in the electronic edition of the journal. A portion is shown here for guidance regarding its form and content.*
[a]Galaxy adversely affected by a very bright star.
[b]Galaxy adversely affected by very crowded field stars.
[c]Galaxy has unreliable sky value determined from model fitting.
[d]Galaxy distorted by an interacting neighbor.
[e]No magnitude zeropoint available.
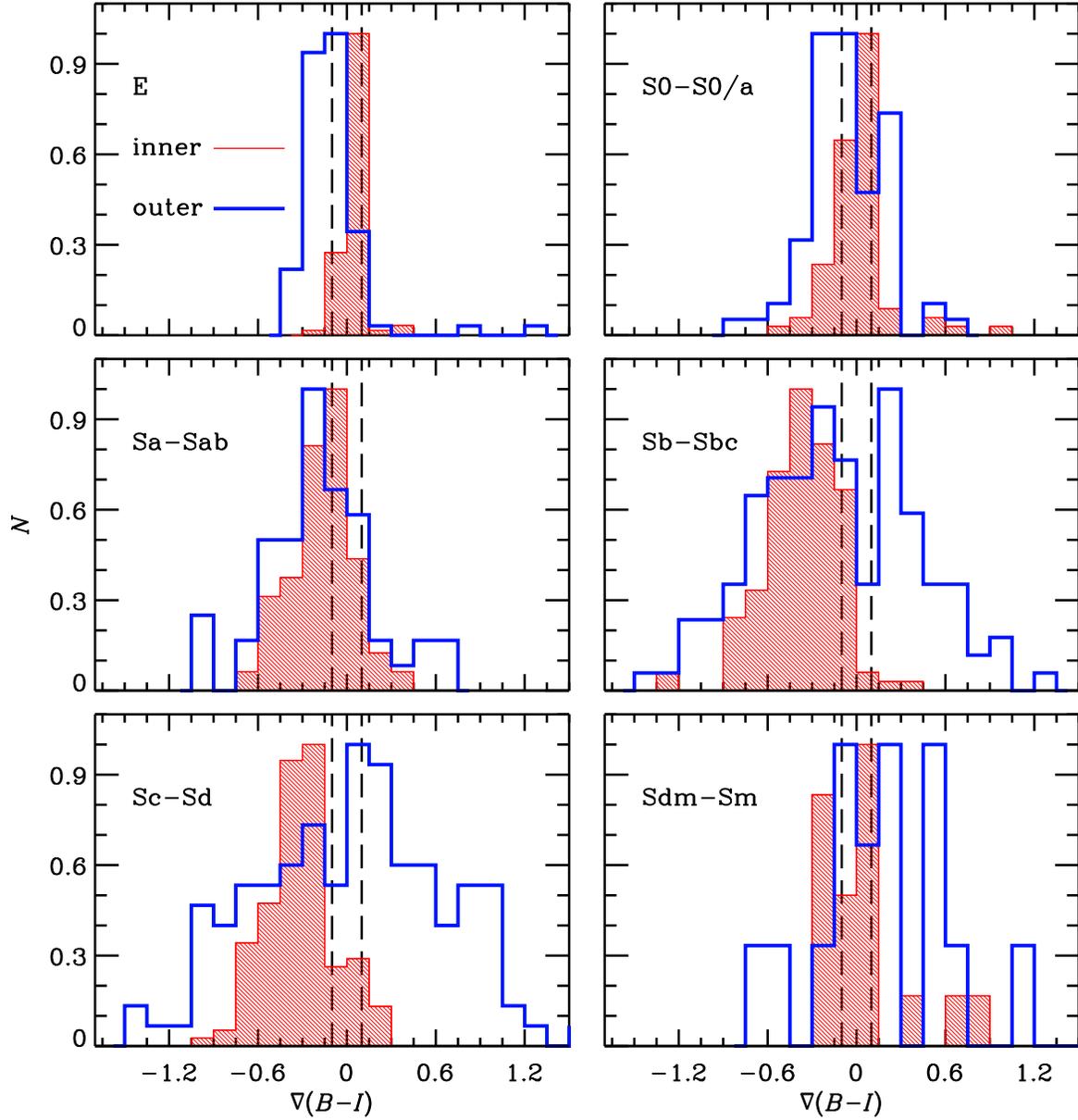
FIG. 6.— Normalized histograms of the inner and outer $B-I$ color gradient, divided by morphological type. The inner and outer color gradients are represented in red and blue solid histograms, respectively. The vertical dashed lines in each panel mark the adopted boundaries for negative ($\nabla(B-I) < -0.1$), flat ($-0.1 \leq \nabla(B-I) \leq 0.1$), and positive ($\nabla(B-I) > 0.1$) color gradients. A positive color gradient means that the color becomes redder outward, while a negative value indicates that the color gets bluer outward.
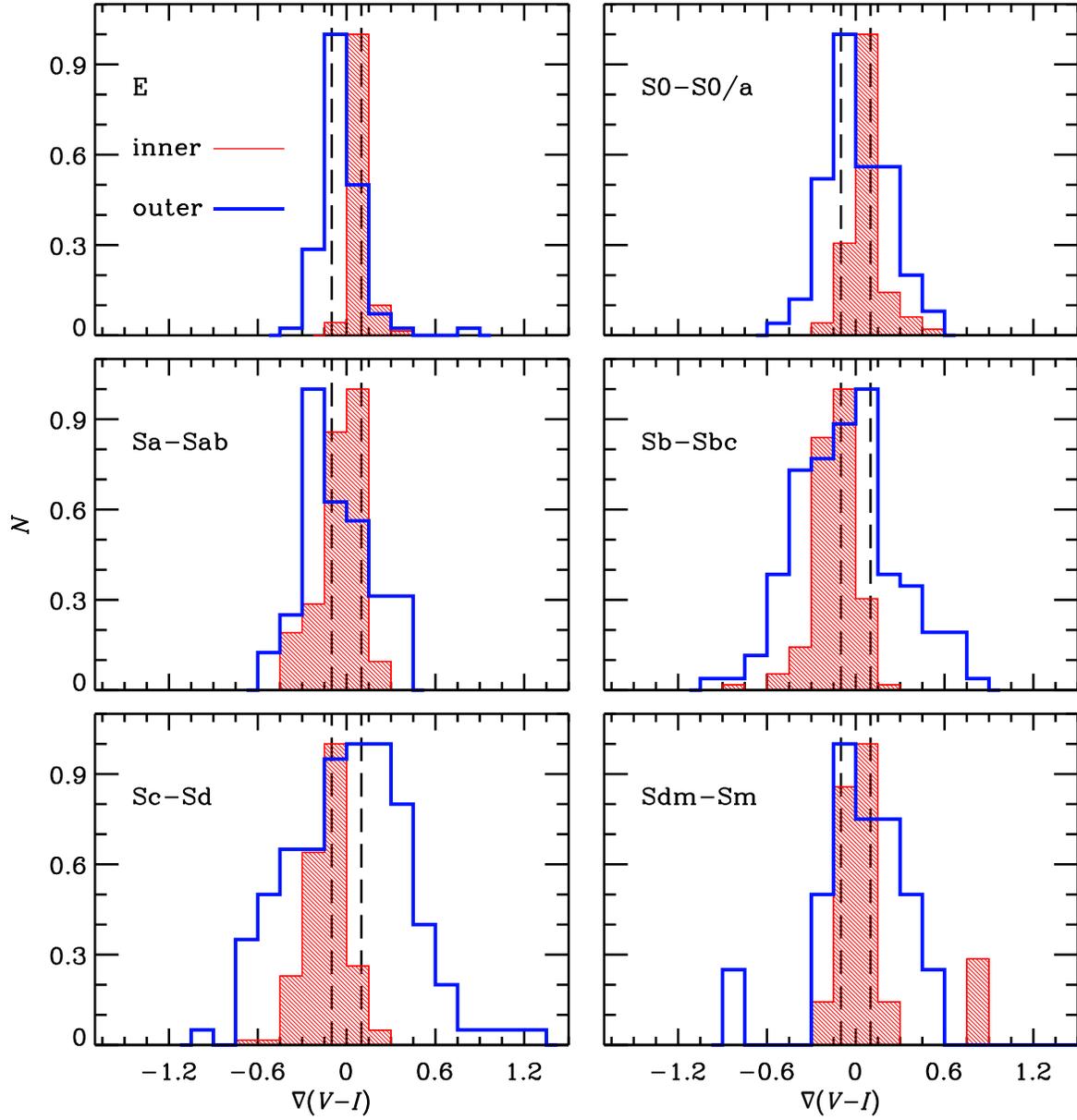
FIG. 7.— Normalized histograms of the inner and outer $V - I$ color gradient. See Figure 6 for details.
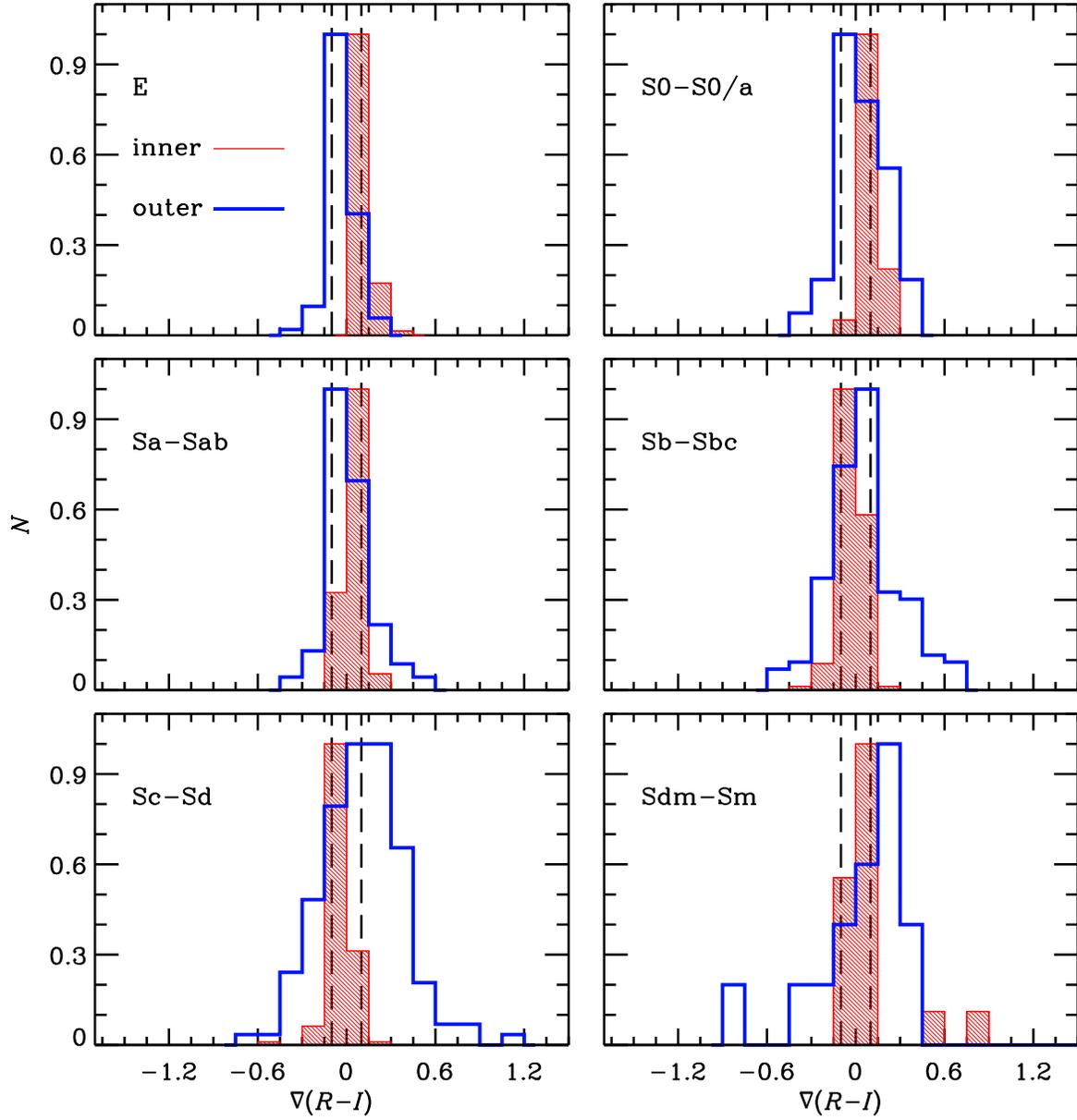
FIG. 8.— Normalized histograms of the inner and outer $R-I$ color gradient. See Figure 6 for details.

Similar to Taylor et al. (2005), the color gradient is derived both inside and outside the half-light radius, R_{50}, as determined in the I band. The inner region ranges from 3 times the seeing FWHM (to avoid spurious effects from seeing mismatches) to R_{50}, while the outer region extends between R_{50} and 2.5 R_{50}. Tests show that most of the color profiles of the CGS galaxies can reach further than 2.5 R_{50}. We confine the color gradient into specific radial ranges marked by the three anchor points for each galaxy[9]. The resulting color profile slope represents the change in color (Δ mag) per dex in radius, where a positive slope indicates that the galaxy is getting redder with increasing radius from its center.

We implement a Monte Carlo method to compute the color gradients and their uncertainties. The essence of our approach is to iteratively sample the two observables, the radius and the color at that radius, while incorporating uncertainties from Poisson noise, sky subtraction, radius measurement, and stochastic fluctuations in the color profile (due to, for instance, substructure from dust lanes, star clusters, or spiral arms). Except for Poisson noise, which is random, the other uncertainties generally contribute to errors in a systematic way. Our Monte Carlo approach makes it possible to derive an effective random uncertainty from a series of systematic errors. We start with the premise that the effective radius is uncertain by a Gaussian error with $\sigma \approx 0.1R_{50}$, which is frequently true when the data are not in the noise-dominated regime. The systematic uncertainty on R_{50} arises from the fact that there is a range of plausible, acceptable models that scatter around the best-fitting solution. We draw a radius from that distribution, and the color at that corresponding radius. The color value is also sampled from a Gaussian distribution given by the Poisson noise, centered on the original color at the sampling radius. The net random uncertainty of the color includes uncertainty in the sky value. The same sampling process is appplied at $2.5R_{50}$, now with an effective scatter of $2.5\sigma(R_{50})$, and in the central region with a scatter of the seeing FWHM. Having sampled the radii and colors around R_0, R_{50}, and $2.5R_{50}$, we calculate the color gradient following

$$\nabla(\text{Color})_{\text{in/out}} = \frac{(\text{Color})_{r_1} - (\text{Color})_{r_0}}{\log r_1 - \log r_0}. \qquad (7)$$

This procedure is repeated 10^4 times to generate a distribution of color, the median and width of which are the gradient and the uncertainty in the gradient, respectively.

Figure 6 shows the normalized histograms of the inner and outer gradients of the $B - I$ color, sorted into bins of different morphological types; the corresponding gradients for the $V - I$ and $R - I$ colors are shown in Figures 7 and 6, respectively. We define positive gradients as those larger than 0.1, flat gradients as those between -0.1 and 0.1, and negative ones as those smaller than -0.1. The vertical dashed lines in each panel mark the boundaries between these three categories.

Table 3 summarizes the statistics for CGS[10]. The color gradients depend strongly on galaxy morphology and color. Elliptical galaxies generally have very little, if any, measurable color gradients. Interestingly, their central regions show a slight tendency to exhibit *positive* gradients in all three colors, whereas beyond their effective radii the trend reverses and there is a mild preference for negative gradients. In either case, the distribution of gradients is narrowly peaked, with a dispersion of ~ 0.11. S0

and S0/a galaxies largely follow the same pattern as the ellipticals. By contrast, spirals of types Sa through Sd behave quite differently. The inner regions of these galaxies show a wide dispersion in gradients (~ 0.23), and they are predominantly negative: the colors get redder toward the center. The gradients in the outer regions, on the other hand, are predominantly flat (peak near 0), and there is roughly an equal number of positive and negative values, although the scatter is large. Galaxies belonging to the latest types (Sdm and Sm) display no preference for gradients of either sign, neither in their interior nor in their exterior regions. The above trends stand out most clearly in $B - I$, the color combination with the greatest wavelength separation, and they become less pronounced in $V - I$, and even more so in $R - I$, although they are still noticeable.

7. BARS

Two fundamental quantities that characterize a bar are its length and strength. There are many ways to estimate the characteristic size of a bar. Apart from simple visual inspection (Kormendy 1979), the most commonly used approaches involve measurement of the maximum value of the bar ellipticity (e.g., Laine et al. 2002; Menéndez-Delmestre et al. 2007), the radial variation of the position angle (e.g., Erwin 2005; Menéndez-Delmestre et al. 2007), the radial variation of the phase angle of the second Fourier mode (Aguerri et al. 2003), and the bar-interbar contrast (Aguerri et al. 2003), as well as direct decomposition of the image into different components (Prieto et al. 1997). The strength of the bar can be ascertained by quantifying the maximum ellipticity in the bar region (Martin 1995; Martinet & Friedli 1997; Menéndez-Delmestre et al. 2007), the torques generated by the bar (Buta & Block 2001), the amplitude of the even Fourier modes of the isophotal intensity distribution (Ohta et al. 1990; Athanassoula & Misiriotis 2002), and direct decomposition of the galaxy into its constituent light fractions (Laurikainen et al. 2005; Gadotti 2008; Peng et al. 2010). Here we present a preliminary appraisal of the bar properties of the CGS sample based on information that can be readily extracted from our 1-D isophotal data. We describe analyses based on the geometric parameters and Fourier components.

7.1. *Geometric Analysis*

In the absence of confusion from dust, star-forming regions, and projection effects, bars usually leave a distinctive imprint on the e and PA profile of a galaxy. The bar is marked by a region wherein the ellipticity rises steadily until it reaches a peak and drops, and, unless the bar semi-major axis is closely aligned with the major axis of the disk, the constant position angle in the bar region abruptly changes value as it transitions into the disk region (Gadotti et al. 2007).

We begin with the e and PA profiles of the I-band image, as extracted from the second step of running the task *ellipse* (§4.1), during which only the galaxy center was held fixed. The I band is preferred over the other bands at shorter wavelengths because it mitigates contamination by dust and young stars. We consider the profiles from an inner radius corresponding to 3 times the seeing disk to the radius where the isophotal intensity is 1σ above the sky background, beyond which we truncate the surface brightness profile. Similar to Menéndez-Delmestre et al. (2007) and Aguerri et al. (2009), bars are required to have a maximum projected ellipticity (e_{max}) greater than 0.2, and

---

[9]In the future, we will also derive the color gradient in physically interesting regions, such as spiral arms, bars, or the break points of the surface brightness profiles.

[10]We excluded the galaxies flagged in Table 2 as adversely affected by field stars.

TABLE 3: FREQUENCY OF COLOR GRADIENTS

| Hubble Type | T | Color | Inner Region | | | Outer Region | | |
| | | | Positive | Flat | Negative | Positive | Flat | Negative |
(1)	(2)	(3)	(4)	(5)	(6)	(7)	(8)	(9)
E	$T < -3$	$B - I$	12.0%	85.5%	2.5%	4.8%	36.1%	59.1%
		$V - I$	58.0%	42.0%	0.0%	13.6%	50.6%	35.8%
		$R - I$	65.9%	34.1%	0.0%	12.2%	65.9%	21.9%
S0–S0/a	$-3 \leq T < 0.5$	$B - I$	16.2%	63.5%	20.3%	27.0%	24.3%	48.7%
		$V - I$	35.1%	57.1%	7.8%	31.2%	33.8%	35.0%
		$R - I$	49.3%	50.7%	0.0%	32.0%	49.3%	18.7%
Sa–Sab	$0.5 \leq T < 2.5$	$B - I$	7.8%	27.5%	64.7%	15.7%	23.5%	60.8%
		$V - I$	9.8%	58.8%	31.4%	23.5%	25.5%	51.0%
		$R - I$	17.6%	78.4%	4.0%	23.5%	52.9%	23.6%
Sb–Sbc	$2.5 \leq T < 4.5$	$B - I$	1.5%	10.7%	87.8%	35.9%	10.7%	53.4%
		$V - I$	2.3%	39.1%	58.6%	27.8%	24.1%	48.1%
		$R - I$	3.0%	85.8%	11.2%	40.3%	33.6%	26.1%
Sc–Sd	$4.5 \leq T < 7.5$	$B - I$	6.0%	8.2%	85.8%	47.0%	10.4%	42.6%
		$V - I$	4.4%	37.0%	58.6%	43.0%	20.0%	37.0%
		$R - I$	3.7%	80.6%	15.7%	50.0%	26.1%	23.9%
Sdm–Sm	$7.5 \leq T < 9.5$	$B - I$	23.5%	41.2%	35.3%	58.8%	17.6%	23.6%
		$V - I$	17.6%	70.6%	11.8%	41.2%	29.4%	29.4%
		$R - I$	12.5%	81.3%	6.2%	50.0%	31.3%	18.7%

NOTE.— Col. (1) Hubble type. Col. (2) Morphological type index. Col. (3) Color. Cols. (4)–(9) Fraction of the positive, flat and negative color gradients in the inner and outer region.

within the bar region the position angle should be constant to within ΔPA $< 20°$. If none of the data points in the e profile exceeds 0.2, or if $\Delta e \leq 0.1$ throughout the entire e profile, we classify the galaxy as unbarred. If $\Delta e > 0.1$ somewhere along the e profile but the associated ΔPA $\leq 10°$, it is possible that a bar exists but happens to align fortuitously with the major axis of the outer disk. We flag these cases as "possibly" barred and carefully inspect the galaxy image visually to see if we can confirm their reality. If the galaxy is barred, we set the inner boundary of the bar region to be the first data point in the e profile that exceeds 0.2. Menéndez-Delmestre et al. (2007) find that near the end of the bar the ellipticity and position angle usually begin to show large deviations, typically at the level of $\Delta e \geq 0.1$ and ΔPA $\geq 10°$. We adopt these criteria to define the radius of the outer boundary of the bar.

The projected bar size is set to be the semi-major axis of the isophote where e peaks (Menéndez-Delmestre et al. 2007), with the associated error as the semi-major axis range containing the tip of the e profile (i.e. $e \geq e_{max} - 0.01$) in the bar region. The reason we do not simply equate the bar size with the outer boundary of the bar is because the change in e and PA in the transition zone between the bar and spiral ams can be influenced by the latter. The outer boundary of the bar can be overestimated if the bar is aligned with the spiral arms. This effect can be mitigated by using the position where e peaks as the bar size, since spiral features cannot produce ellipticity values as high as those of a bar. Assuming that the intrinsic shape of the galaxy disk is purely circular, we correct the observed, projected bar length (R_{bar}^o) to its intrinsic value (R_{bar}^i) following

$$R_{bar}^i = R_{bar}^o \sqrt{(\cos\Delta\text{PA})^2 + \left(\frac{\sin\Delta\text{PA}}{1 - e_{gal}}\right)^2}, \qquad (8)$$

where ΔPA $=$ PA$_{gal}$ $-$ PA$_{bar}$, and PA$_{gal}$ and e_{gal} are the position angle and ellipticity of the outer disk of the galaxy. Although a full 2-D analytical deprojection of the bar is more accurate (see Appendix A in Gadotti et al. 2007), in practice the size estimates from the two methods agree very well. The typical difference in bar radii measured by 1-D fitting compared to 2-D deprojection is about $0''3$. Since the difference is very small, we use the 1-D method for simplicity. The projected e_{max} then represents the strength of the bar (Menéndez-Delmestre et al. 2007), with the fitted error of e_{max} as its uncertainty. The position angle of the bar, PA$_{bar}$, is given by the average PA over the bar region, with the RMS as its error.

Figure 9 illustrates how we identify and measure the bar size and strength, as applied to the star-cleaned I-band image of the SBb galaxy NGC 7513. The radial profiles of e and PA clearly show the hallmark features of a bar: a distinctly broad peak in e above our minimum threshold of 0.2, reaching $e_{max} = 0.68$, and an extended plateau of near-constant PA $\approx 75°$ (ΔPA $\leq 20°$). The outer disk of the galaxy has a clearly different e (0.33) and PA (105°). The two vertical solid lines mark the inner and outer boundary of the bar-dominated region; the vertical dotted line gives the projected bar radius. Although widely used in the literature, the measured e_{max} of the bar is actually ~ 20 percent lower than that derived from 2-D image decomposition when the bulge and disk components are also included (Gadotti 2008). Indeed, reliable bar parameters can only be determined
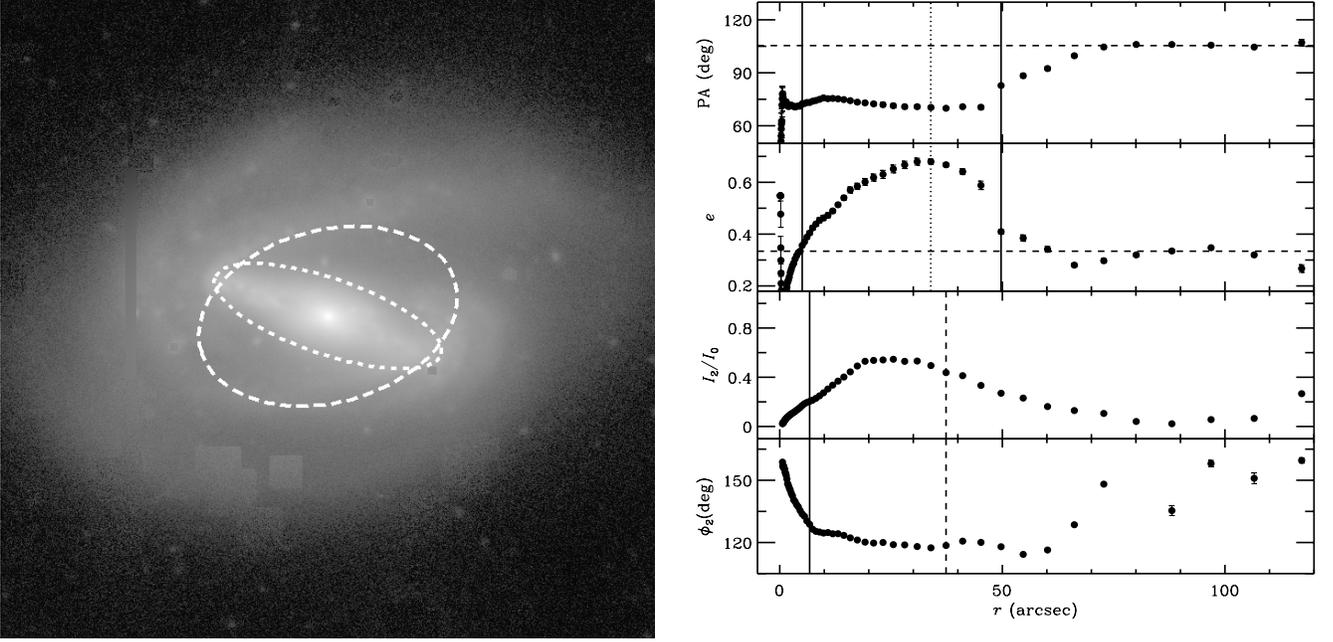
FIG. 9.— Illustration of how we determine the size and strength of a bar. (*Left*) Star-cleaned *I*-band image of NGC 7513; the size of the image is ~3′×3′. (*Right*) Radial profiles of PA, *e*, I_2/I_0, and ϕ_2. The horizontal dashed lines in the PA and *e* panels denote the characteristic values of the galaxy. The solid vertical lines mark the inner and outer boundary of the bar-dominated region, and the dotted vertical line represents the projected size of the bar determined using the geometric method, where the bar is required to have $e_{max} \geq 0.2$ and $\Delta PA \leq 20°$. In the I_2/I_0 and ϕ_2 panels, the solid vertical line marks the inner boundary of the bar. The vertical dashed line represents both the outer boundary and size of the bar, determined using the Fourier method, where the bar criteria are $I_2/I_0 \geq 0.2$ and $\Delta\phi_2 \leq 20°$. The corresponding isophotal ellipses for the two methods are overplotted on the left-hand image with the same type of lines as in the right-hand panel.
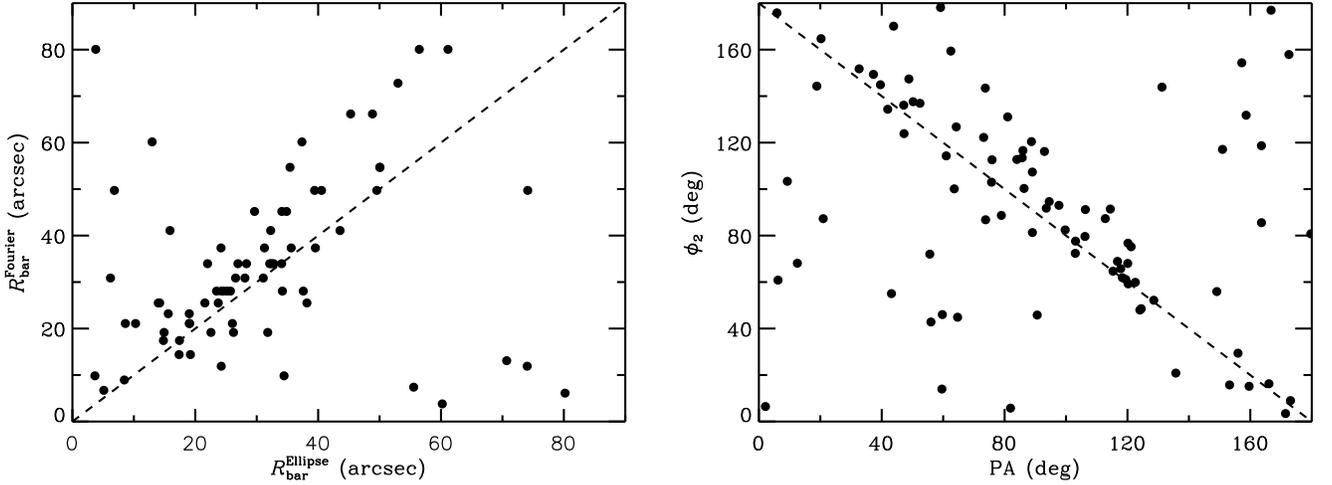
FIG. 10.— (*Left*) Correlation between $R_{bar}^{Ellipse}$, the deprojected bar size measured from the geometric, ellipse method and $R_{bar}^{Fourier}$, that measured from the Fourier decomposition. The dashed line represents $y = x$. (*Right*) Correlation between ϕ_2 and PA of the bar. The dashed line represents $y = 180° - x$.

by 2-D decomposition of the images with all of the other components included. Such analysis is outside the scope of this work, but future papers will present results from 2-D decompositions of the CGS images.

7.2. *Fourier Analysis*

In addition to the geometric method described above, we also derive bar properties using the radial profiles of the relative amplitude of the $m = 2$ Fourier mode (I_2/I_0) and its associated phase angle (ϕ_2). As before, we work with the *I*-band images. Bars are usually associated with the first local maximum in the I_2/I_0 profile, where the bar/inter-bar contrast is largest, over an

extended region where ϕ_2 keeps approximately constant. Subsequent maxima in the I_2/I_0 profile, if present, trace spiral arms or ring structures, but in these instances ϕ_2 varies with radius. Spiral arms always produce varying phase angles, and thus the region where they dominate can be easily excluded from the bar size measurement.

Adopting a procedure similar to that used by Aguerri et al. (2009), we define the bar to be the region wherein the maximum relative $m = 2$ Fourier amplitude $(I_2/I_0)_{max} > 0.2$ and the phase angle remains constant to $\Delta\phi_2 < 20°$. We set the inner boundary of the bar to be the first data point outside of 3 times the seeing radius in which $I_2/I_0 > 0.2$. Past the peak, we

TABLE 4: PROPERTIES OF BARS

Name	Flag	R^i_{bar} ($''$)	e_{bar}	$\mathrm{PA}_{\mathrm{bar}}$ ($°$)	$(I_2/I_0)_{\mathrm{bar}}$	$(\phi_2)_{\mathrm{bar}}$ ($°$)	Notes
(1)	(2)	(3)	(4)	(5)	(6)	(7)	(8)
ESO 009-G010	N	$\cdots$	$\cdots$	$\cdots$	$\cdots$	$\cdots$	
ESO 027-G001	B	23.74 ± 4.45	0.50 ± 0.02	64.25 ± 3.77	0.38 ± 0.04	126.77 ± 6.04	
ESO 027-G008	N	$\cdots$	$\cdots$	$\cdots$	$\cdots$	$\cdots$	extra
ESO 056-G115	N	$\cdots$	$\cdots$	$\cdots$	$\cdots$	$\cdots$	$BVRI^{\mathrm{c}}$
ESO 060-G019[a]	B	20.43 ± 3.00	0.38 ± 0.02	28.58 ± 5.00	0.76 ± 0.03	145.03 ± 5.56	
ESO 091-G003	N	$\cdots$	$\cdots$	$\cdots$	$\cdots$	$\cdots$	extra
ESO 097-G013	N	$\cdots$	$\cdots$	$\cdots$	$\cdots$	$\cdots$	$BVRI^{\mathrm{c}}$
ESO 121-G006	N	$\cdots$	$\cdots$	$\cdots$	$\cdots$	$\cdots$	I^{b}
ESO 121-G026	B	19.21 ± 2.26	0.57 ± 0.01	166.75 ± 11.08	0.55 ± 0.03	176.96 ± 1.45	
ESO 136-G012	N	$\cdots$	$\cdots$	$\cdots$	$\cdots$	$\cdots$	$BVRI^{\mathrm{c}}$

NOTE.— Col. (1) Galaxy name. Col. (2) Flag indicating whether the galaxy is barred: "B" = barred; "B:" = possibly barred; "N" = not barred. Col. (3) Bar radius (intrinsic, deprojected according to Equation 7). Col. (4) Bar ellipticity. Col. (5) Position angle of the bar, east of north. Col. (6) Relative amplitude of the $m = 2$ mode of the bar. Col. (7) Phase angle of the $m = 2$ mode of the bar. Col. (8) Notes: "extra" = object not formally part of the main sample; filters = image of that filter has problem, which is indicated by the table mark. *Table 4: Properties of Bars is presented in its entirety in the electronic edition of the journal. A portion is shown here for guidance regarding its form and content.*
[a] The size, e, and PA are determined by eye.
[b] Galaxy adversely affected by a very bright star.
[c] Galaxy adversely affected by very crowded field stars.
[d] Galaxy distorted by an interacting neighbor.

designate the radius where $I_2/I_0 = (I_2/I_0)_{\mathrm{max}} - 0.1$ as the outer boundary of the bar region. In the event that there is a secondary maximum and the local minimum between the two peaks exceeds $(I_2/I_0)_{\mathrm{max}} - 0.1$, we set the position of the local minimum to be the outer boundary of the bar region.

We assign $(I_2/I_0)_{\mathrm{max}}$ to be the bar strength, with the uncertainty set by the statistical error derived from the Fourier decomposition process. As the Fourier method is minimally affected by spiral arms, we simply set the bar size to be equal to the radius of its outer boundary; its associated uncertainty is the semi-major axis range between the outer boundary and the radius where $I_2/I_0 = (I_2/I_0)_{\mathrm{max}} - 0.05$. The Fourier analysis is performed on the isophotes extracted in the third step of the ellipse fitting, where the geometric parameters were all fixed to those of the outermost isophote (see §4.1). For simplicity, we just assume that the disk is purely circular in its face-on view, so the semi-major axes of the isophotal ellipses are the radii of the circles. The size of the bar is denoted by the semi-major axis of the particular isophote that encloses the bar region, which is actually the radius of the circle that passes right through the end of the bar in a face-on view. Under this simplified assumption, the bar size is already deprojected. The characteristic phase angle of the bar is the average ϕ_2 within the bar region, with $\Delta\phi_2$ as the uncertainty. The two bottom-right panels of Figure 9 show our Fourier technique applied to NGC 7513.

Fourier analysis offers a very useful approach to studying bars. It not only provides another independent method to identify and quantify bars, but also recovers bars missed by the geometric method in galaxies with internal structure too complex to yield an unambiguous bar signature in their e and PA profiles. In fact, the bar parameters derived from these two methods usually agree quite well. Figure 10 (left panel) compares the bar sizes measured from the ellipse method ($R^{\mathrm{Ellipse}}_{\mathrm{bar}}$; deprojected) versus those measured from the Fourier method ($R^{\mathrm{Fourier}}_{\mathrm{bar}}$). Overall, there is a good correlation, but some glaring outliers stand out. Although our analysis is done in the I

band, dust extinction can still be significant in some galaxies. The dust extinction features near the central region of a galaxy tends to trick the Fourier method by producing a false peak in I_2/I_0 with roughly constant ϕ_2; this yields an unusually compact, incorrect bar size. The Fourier method can also be unreliable for weak bars embedded in disks with strong spiral arms. Under these circumstances, the relatively weak local peak of the bar in the I_2/I_0 profile can be overshadowed by a stronger peak generated by the spiral arms, leading to an overestimate of the bar size. The position angle of the bar correlates strongly with ϕ_2 (Figure 10, right panel). Ideally, $\phi_2 = 180° - \mathrm{PA}$. However, when the PA of the bar approaches $0°$ or $180°$, the corresponding phase angle can have values similar to the PA; this is responsible for the points lying on the lower-left and upper-right portions of the figure. Dust in the central regions of the galaxy further contributes to the scatter.

7.3. *Final Bar Classification*

Since neither of the methods discussed above is foolproof, we use both to assign the final bar classification to the galaxies in CGS. If a galaxy is not classified as barred in both the geometric and Fourier analysis, it is labeled unbarred. If the galaxy is classified as barred by only one method, we call it "possibly" barred. If both methods consider a galaxy barred, we check whether the derived bar sizes are consistent between them. We only classify it as definitely barred if the bar sizes from the two methods differ by less than $10''$; if they disagree by more than $10''$, we call it "possibly" barred.

For the "possibly" barred galaxies, we visually examine their I-band images and further scrutinize their geometric and Fourier profiles to check whether we are being misled by internal structural complexities such as spiral arms or dust features. If any of the measurements from either of the two methods is suspect, we manually set the inner and outer boundary of the bar region and redo the measurements. Not all ambiguous cases can be resolved, and in our final classification we continue to
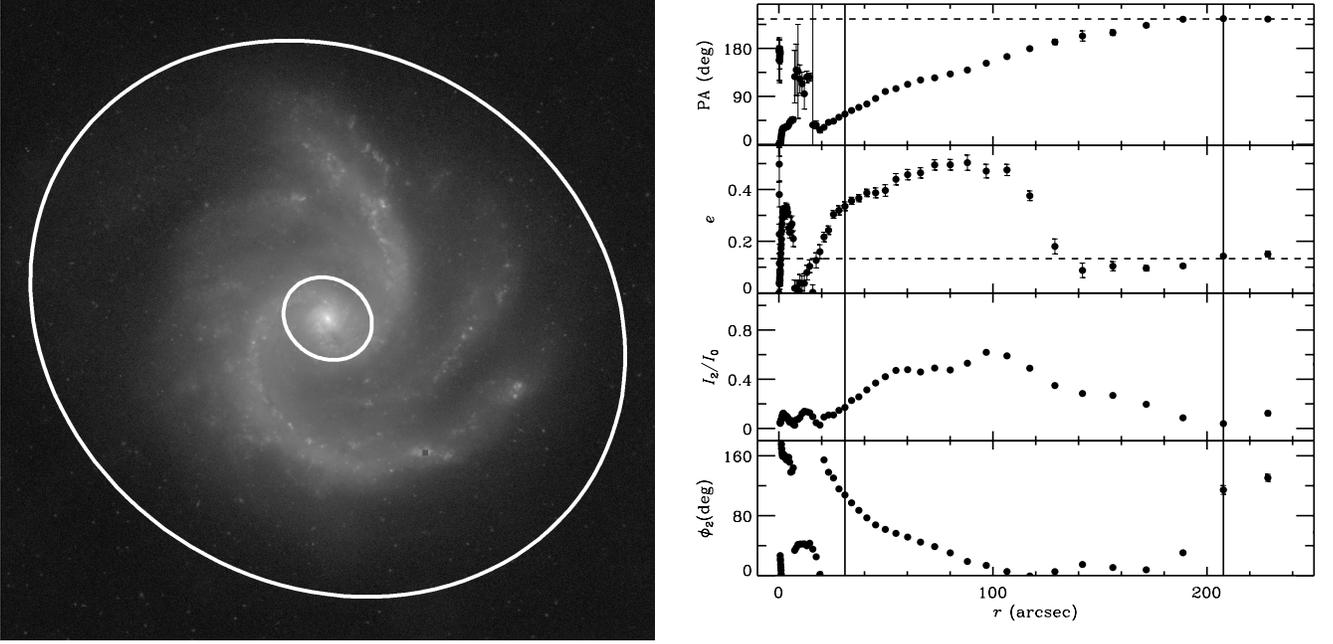
FIG. 11.— Illustration of how we measure the strength of the spiral arms using the Fourier method. (*Left*) Star-cleaned *I*-band image of NGC 5247; the size of the image is $\sim 7\rlap{.}'3 \times 7\rlap{.}'3$. (*Right*) Radial profiles of PA, e, I_2/I_0, and ϕ_2. The solid vertical lines mark the inner and outer boundary of the disk-dominated region, which is defined to be outside the central bulge or bar component, but inside the radius where the isophotal intensity is 3 σ above the sky background. The corresponding isophotal ellipses are overplotted on the left-hand image. The horizontal dashed lines in the PA and e panels denote the characteristic values of the galaxy.
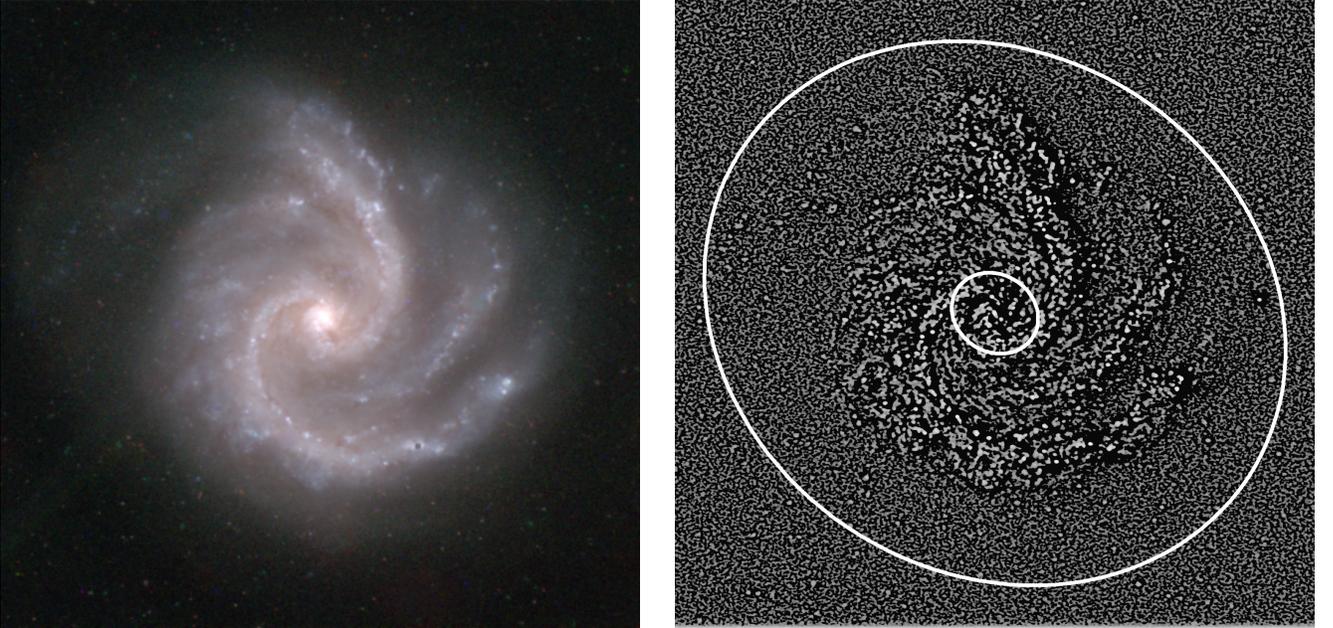
FIG. 12.— Illustration of how we measure the strength of the spiral arms using the structure map. (*Left*) Star-cleaned composite color image of NGC 5247; the size of the image is $\sim 7\rlap{.}'3 \times 7\rlap{.}'3$. (*Right*) Structure map of the star-cleaned *B*-band image. The two overplotted ellipses mark the inner and outer boundaries where the spiral arms populate. After rejecting the masked objects, we use the RMS of the pixels within these two ellipses to estimate the strength of the spiral arms.

flag their bar status as uncertain. For our final measurement of the bar size, we usually give higher priority to the results derived from the geometric method, which generally gives more accurate sizes than those derived from the Fourier method. The definition of the bar size in the Fourier method is of limited utility because it is largely arbitrary and more prone to being influenced by the presence of spiral arms. Table 4 summarizes the final bar classification and some basic bar parameters derived from our analysis. Among the 501 disk galaxies ($T \geq -3$)

in the final catalog, 44 (9%) are deemed definitely barred, 136 as possibly barred (27%), and 321 (64%) as unbarred. As bar identification is uncertain in highly inclined galaxies, we reexamine the statistics in a subsample restricted to have ellipticities smaller than $e_{\rm gal} = 0.6$. As expected, the bar fraction increases. Out of 387 disk galaxies, 173 (45%) are barred and 214 (55%) are unbarred. A more detailed comparison between our results and those in the literature will be deferred to a future paper.

TABLE 5: PROPERTIES OF SPIRAL FEATURES

Name (1)	$\langle I_2/I_0\rangle_B$ (2)	$\langle I_2/I_0\rangle_V$ (3)	$\langle I_2/I_0\rangle_R$ (4)	$\langle I_2/I_0\rangle_I$ (5)	σ_s^B (6)	σ_s^V (7)	σ_s^R (8)	σ_s^I (9)	Notes (10)
ESO 009-G010	0.11±0.08	0.09±0.07	0.08±0.06	0.07±0.05	0.006	0.004	0.003	0.002	
ESO 027-G001	0.31±0.21	0.29±0.20	0.28±0.21	0.27±0.23	0.008	0.008	0.005	0.002	
ESO 027-G008	0.23±0.19	0.22±0.18	0.23±0.18	0.23±0.20	0.010	0.008	0.007	0.003	extra
ESO 056-G115	⋯	⋯	⋯	⋯	⋯	⋯	⋯	⋯	$BVRI$[b]
ESO 060-G019	0.55±0.24	0.50±0.23	0.48±0.21	0.48±0.16	0.044	0.038	0.048	0.037	
ESO 091-G003	0.10±0.06	0.11±0.06	0.11±0.07	0.12±0.08	0.008	0.008	0.005	0.003	extra
ESO 097-G013	⋯	⋯	⋯	⋯	⋯	⋯	⋯	⋯	$BVRI$[b]
ESO 121-G006	0.25±0.22	0.24±0.20	0.22±0.17	0.18±0.10	0.009	0.020	0.027	0.025	I[a]
ESO 121-G026	0.20±0.09	0.19±0.09	0.19±0.08	0.17±0.07	0.010	0.008	0.007	0.003	
ESO 136-G012	0.22±0.07	0.33±0.58	0.23±0.28	0.19±0.15	0.013	0.017	0.016	0.008	$BVRI$[b]

NOTE.— Col. (1) Galaxy name. Cols. (2)–(5) Average value of I_2/I_0 within the disk-dominated region of the B, V, R, and I-band images, respectively. Cols. (6)–(9) Standard deviation of the pixels within the disk-dominated region of the structure maps of the B, V, R, and I-band images, respectively. Col. (10) Notes: "extra" = object not formally part of the main sample; filters = image of that filter has problem, which is indicated by the table mark. *Table 5: Properties of Spiral Features is presented in its entirety in the electronic edition of the journal. A portion is shown here for guidance regarding its form and content.*
[a]Galaxy adversely affected by a very bright star.
[b]Galaxy adversely affected by very crowded field stars.
[c]Galaxy distorted by an interacting neighbor.

8. SPIRAL ARMS

We provide two quantitative measurements (Table 5) that can be used to access the presence and strength of spiral arms in galaxies. The analysis is applied uniformly to all non-elliptical galaxies in the sample, including disk galaxies traditionally deemed to lack spiral arms, such as S0s.

We perform a simple measurement of the average strength of I_2/I_0 in the disk region outside the central bulge and the bar. Spiral arms are the main contributor to any significant $m = 2$ mode in this region[11]. If neither a featureless, classical bulge nor a bar is present, the minimum inner boundary for our calculation is set to 3 times the seeing radius. For barred galaxies, the inner boundary is naturally set to the bar radius, which almost always lies exterior to the bulge. For unbarred galaxies with classical bulges, we define the inner boundary to be the radius where $e > 0.2$, beyond which the disk usually dominates over the bulge. This criterion fails for face-on galaxies with very weak spiral arms and classical bulges, because the disk becomes indistinguishable from the bulge on the basis of its ellipticity alone. Fortunately, under these circumstances both the bulge and the disk contribute little to I_2/I_0 anyway, and it makes little difference whether the bulge is excluded or not. The outer boundary is the radius where the isophotal intensity reaches 3σ above the background in the I-band image; we apply the same boundary for the other filters. We then calculate a characteristic value of I_2/I_0 by averaging its profile between the inner and outer boundary. We illustrate our methodology in Figure 11, applied to the Sbc galaxy NGC 5247.

Our second method makes use of the structure maps (Paper I) to estimate the strength of the spiral features (Figure 12). After masking out the field stars and background galaxies, we compute the standard deviation of all the remaining pixels within the inner and outer boundaries of the disk-dominated region, as determined above. The agreement between the two different

measurements is not good, as can be seen in Figure 13, where we plot $\langle I_2/I_0\rangle$ against σ_s for all the filters. The two parameters trace structures on different scales. The structure map optimally filters spatial features on the scale of the point-spread function. It effectively highlights features such as dust lanes and thin arms, but it is not very sensitive to smooth and wide spiral arms, which can be better probed via $\langle I_2/I_0\rangle$.

9. LOPSIDEDNESS

The relative amplitude of the $m = 1$ Fourier mode is widely used to study the lopsidedness of galactic stellar (Rix & Zaritsky 1995; Zaritsky & Rix 1997; Bournaud et al. 2005; Jog & Combes 2008; Reichard et al. 2008) and gaseous (e.g., van Eymeren et al. 2011) disks. This approach is well-defined, quantitative, and relatively straightforward to implement, and hence can be applied to study large samples of galaxies. A lopsided disk stands out as a region of enhanced I_1/I_0 and roughly constant phase angle ϕ_1. A one-arm spiral also exhibits a large I_1/I_0, but ϕ_1 increases monotonically as a function of radius.

Our method to measure lopsidedness differs somewhat from that used in previous works. Rix & Zaritsky (1995) perform a bulge-to-disk decomposition of the surface brightness profile to determine the scale length of the disk, and then compute the average relative Fourier amplitude between 1.5 and 2.5 scale lengths. As we do not yet have robust structural decompositions for the entire CGS sample (this work is in progress), we resort to a simpler strategy, one based on the expectation that the lopsided portion of the disk should be characterized by a roughly flat ϕ_1 radial profile. Through careful experimentation with a number of galaxies with prominent lopsided disks, we find that the lopsided region can be effectively isolated by requiring that the phase angle be constant to within $\Delta\phi_1 \leq 70°$. We apply this criterion to the phase angle profile of the I-band image to define the inner and outer radii of the lopsided region,

---

[11]The $m = 2$ mode is most sensitive to systems with grand design, two-arm spirals. However, flocculent or multiple-arm spirals still exhibit significant amplitude in the $m = 2$ mode. We defer a full treatment of spiral arms, including exploration of high-order modes, to a separate paper.
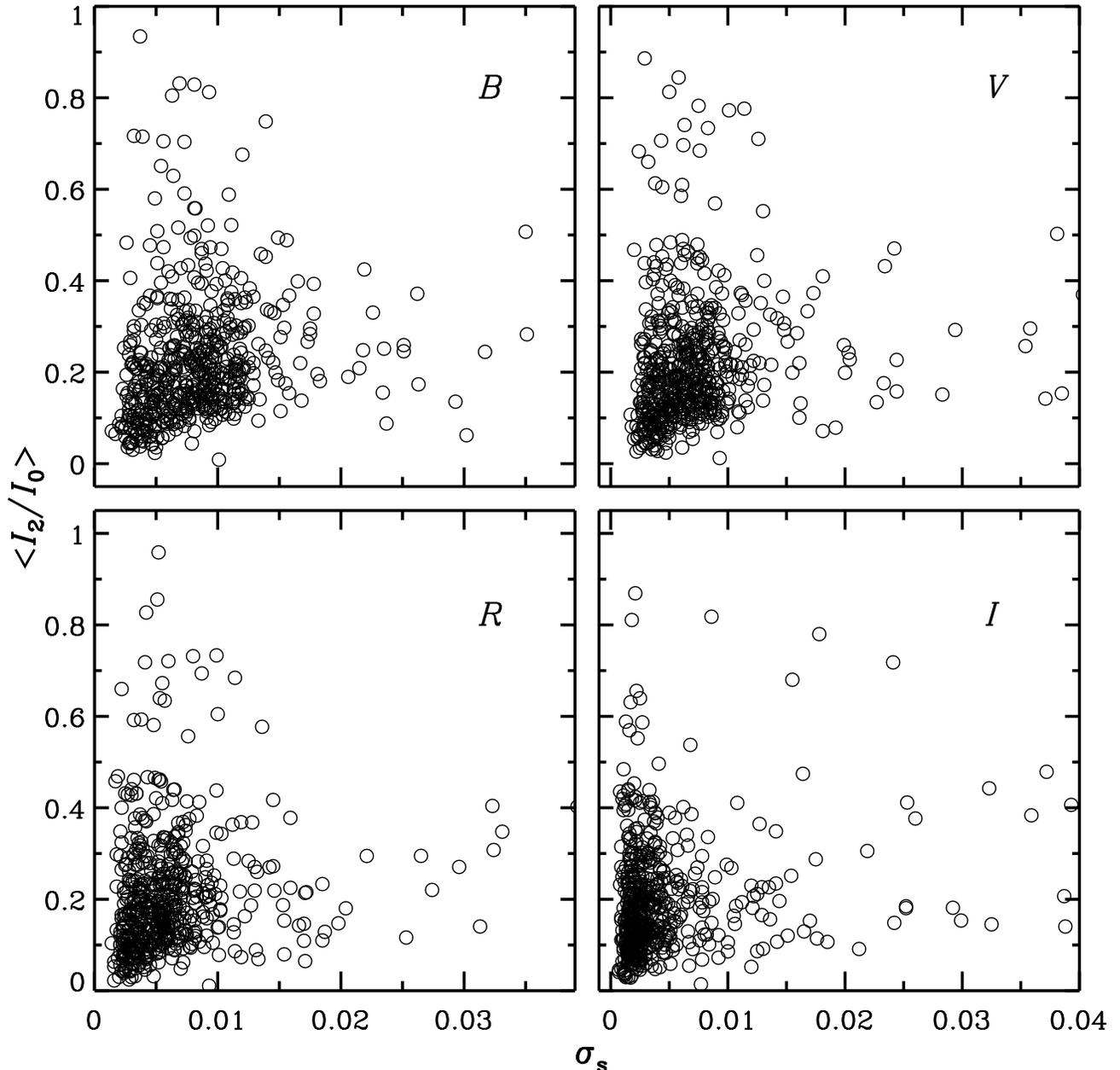
FIG. 13.— Comparison between the two measures of the spiral arms ($\langle I_2/I_0 \rangle$ and σ_s) for *BVRI* filters. The correlation is very weak or absent, because the two measures essentially probe structures on quite different scales. σ_s is mainly determined by structures with typical scales of the point-spread function, while $\langle I_2/I_0 \rangle$ is more sensitive to more extended, large-scale features coherent over significant portions of the spiral arms.

and then adopt these values for the other filters. For each filter, the lopsidedness is the average value of I_1/I_0 within that region, with the standard deviation as its associated uncertainty. The characteristic value of ϕ_1 and its error are calculated similarly. Figure 14 illustrates our method on the Scd galaxy NGC 7070.

Lopsidedness measurements for the entire sample are given in Table 6[12]. Table 7 summarizes the frequency of galaxies with significant lopsidedness, defined as $\langle I_1/I_0 \rangle_I \geq 0.2$ (e.g., Zaritsky & Rix 1997), for the subsample of 350 disk galaxies with $e_{gal} \leq 0.6$ for which robust measurements could be made. Consistent with previous studies, the fraction of galaxies with sig-

nificant lopsidedness is high, and the frequency increases substantially in late-type galaxies.

10. DATA VERIFICATION

10.1. *Internal Comparison*

Several galaxies were observed more than once during different nights throughout the survey. Although only the best images are included in the final CGS catalog, the repeat observations, which were reduced and analyzed in the same manner as the rest, afford an opportunity to access the accuracy of our calibration methods and the reliability of the parameter measurements.

[12]We have flagged the galaxies whose lopsidedness measurements may be unreliable because of contamination by bright stars or excessive crowding by field stars.
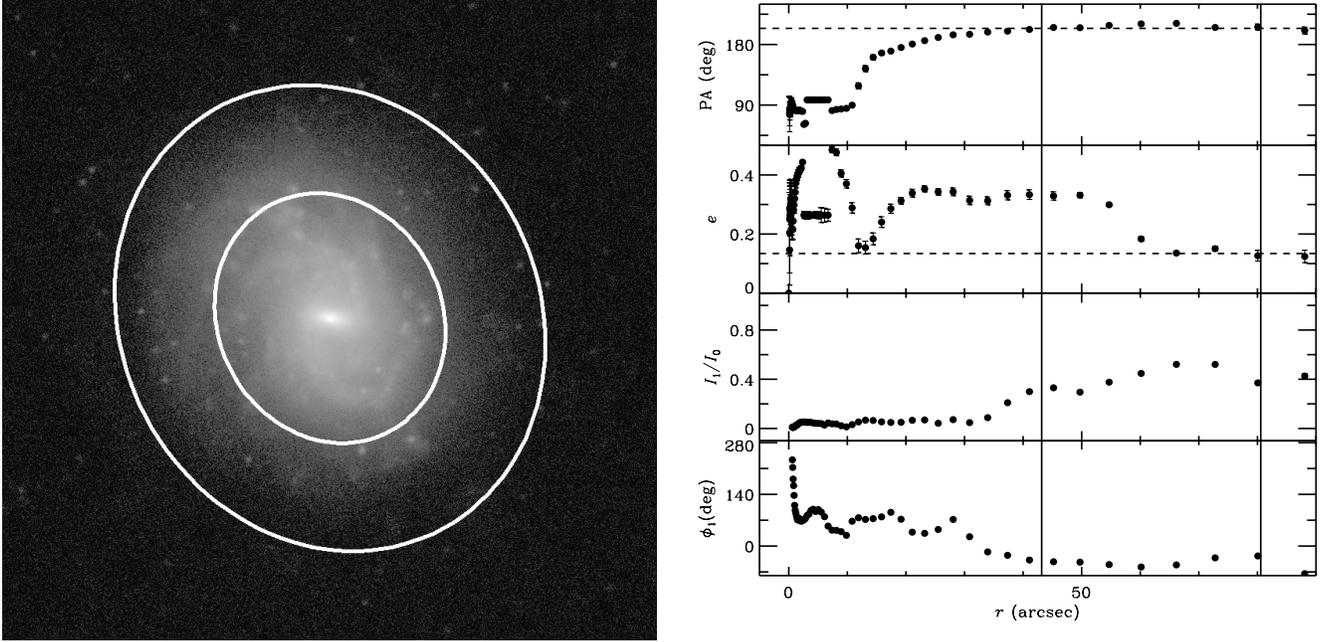
FIG. 14.— Illustration of how we measure lopsidedness. (*Left*) Star-cleaned *I*-band image of NGC 7070; the size of the image is $\sim3'.6\times3'.6$. (*Right*) Radial profiles of PA, e, I_1/I_0, and ϕ_1. The horizontal dashed lines in the PA and e panels denote the characteristic values of the galaxy. The solid vertical lines, and the corresponding isophotal ellipses overplotted on the left-hand image, mark the inner and outer boundary of the region used to compute the lopsidedness, which we define to be that in which the radial variation of ϕ_1 is smaller than $70°$. The lopsidedness is measured simply by averaging I_1/I_0 within this region.

TABLE 6: LOPSIDEDNESS MEASUREMENTS

Name (1)	$\langle\phi_1\rangle_I$ (2)	$\langle I_1/I_0\rangle_B$ (3)	$\langle I_1/I_0\rangle_V$ (4)	$\langle I_1/I_0\rangle_R$ (5)	$\langle I_1/I_0\rangle_I$ (6)	Notes (7)
ESO 009-G010	338.5±9.9	0.20±0.10	0.16±0.09	0.16±0.09	0.15±0.10	
ESO 027-G001	70.4±4.0	0.53±0.14	0.50±0.14	0.48±0.12	0.45±0.11	
ESO 027-G008	168.9±2.3	0.13±0.03	0.10±0.03	0.14±0.05	0.21±0.13	extra
ESO 056-G115	⋯	⋯	⋯	⋯	⋯	$BVRI^{\rm b}$
ESO 060-G019	240.0±11.6	0.12±0.10	0.18±0.08	0.16±0.05	0.19±0.05	
ESO 091-G003	11.0±17.4	0.10±0.04	0.09±0.02	0.10±0.04	0.17±0.09	extra
ESO 097-G013	⋯	⋯	⋯	⋯	⋯	$BVRI^{\rm b}$
ESO 121-G006	226.3±18.4	0.25±0.09	0.29±0.12	0.28±0.07	0.17±0.06	$I^{\rm a}$
ESO 121-G026	161.0±19.6	0.30±0.13	0.35±0.15	0.34±0.15	0.29±0.14	
ESO 136-G012	155.3±17.0	0.23±0.19	1.01±1.62	0.42±0.58	0.28±0.25	$BVRI^{\rm b}$

NOTE.— Col. (1) Galaxy name. Col. (2) Phase angle (in units of degrees) of the lopsided region in the *I*-band image. Cols. (3)–(6) Strength of the lopsidedness parameter for the B, V, R, and *I*-band images, respectively. Col. (7) Notes: "extra" = object not formally part of the main sample; filters = image of that filter has problem, which is indicated by the table mark. *Table 6: Lopsidedness Measurements is presented in its entirety in the electronic edition of the journal. A portion is shown here for guidance regarding its form and content.*
[a]Galaxy adversely affected by a very bright star.
[b]Galaxy adversely affected by very crowded field stars.
[c]Galaxy distorted by an interacting neighbor.

Table 8 lists the galaxies that have pairs of repeat observations useful for internal comparison. Note that for this exercise we only select objects that have reasonably good data. Many of the duplicate observations were taken precisely because the original observation was deemed to be of exceptionally low quality, either because of weather conditions (bad seeing, excessive cloud cover) or technical problems (poor telescope focus, tracking errors). Because one of the observations in the comparison pair is—by definition—suboptimal, the following

assessment, in some sense, gives an overly conservative estimate of the magnitude of internal errors.

Figure 15 compares the surface brightness profiles for galaxies observed on different nights. In most cases, they agree quite well. The weighted average of the profile differences (dashed line, calculated by averaging the profile differences weighted by the corresponding error at each data point) resides well inside the formal 1σ photometric uncertainty (Noordermeer & van der Hulst 2007). This suggests that our photometric errors

TABLE 7: Frequency of Significant Lopsidedness

Hubble Type (1)	T (2)	Number (3)	Fraction (4)
S0–S0/a	$-3 \leq T < 0.5$	77	15.6%
Sa–Sab	$0.5 \leq T < 2.5$	48	25.0%
Sb–Sbc	$2.5 \leq T < 4.5$	110	45.5%
Sc–Sd	$4.5 \leq T < 7.5$	103	64.1%
Sdm–Sm	$7.5 \leq T < 9.5$	12	83.3%

NOTE.— Col. (1) Hubble type. Col. (2) Morphological type index. Col. (3) Number of objects. Col. (4) Fraction of galaxies with significant lopsidedness, defined to be those with $\langle I_1/I_0 \rangle_I \geq 0.2$ in the I-band.

are robust, both for the photometric and nonphotometric observations. A few objects (NGC 1374, 2196, 6810, 6861, 7590) show slightly larger, but by no means alarming, discrepancies. Two types of differences in profile *shape* can be seen. The innermost portions of the profiles often show systematic deviations, sometimes as large as ~ 0.5 mag arcsec^{-2}. This effect can be entirely attributed to mismatches in seeing, but is well confined within ~ 3 times the radius of the seeing disk. This is the reason we restrict all of our scientific analysis to radii beyond this. Additionally, many of the profiles show some level of systematic deviation at large radii. This most likely arises from errors in sky subtraction. For most objects, the deviations occur at the level of ~ 0.2 mag arcsec^{-2}, but they lie well within the error bars of the individual isophotal intensities, which again indicates that our error budget is realistic. The most extreme deviations occur in galaxies that are too extended for standard sky subtraction, for which we had to resort to an indirect estimate based on profile fitting (Section 3). In these cases, the deviations in the outer profiles may be as large as ~ 0.5 mag arcsec^{-2}. NGC 2434 is such an example. However, our formal error bars appear to be realistic even in these extreme situations.

TABLE 8: Internal Comparison Sample

Name (1)	Filter (2)	Date 1 (yyyy-mm-dd) (3)	Conditions 1 (4)	Date 2 (yyyy-mm-dd) (5)	Conditions 2 (6)
ESO 311-G012	$BVRI$	2006-01-28	N	2004-01-18	N
IC 2597	$BVRI$	2006-01-27	N	2004-04-16	N
NGC 1374	VI	2003-11-20	N	2003-11-22	P
NGC 1399	$BVRI$	2006-01-27	N	2003-11-18	N
NGC 1688	$BVRI$	2006-01-28	N	2004-01-17	N
NGC 1700	$BVRI$	2006-01-27	N	2003-11-20	N
NGC 2196	$BVRI$	2006-01-29	N	2003-02-09	N
NGC 2310	$BVRI$	2006-01-29	N	2004-01-18	N
NGC 2434	$BVRI$	2006-01-26	N	2003-11-20	N
NGC 2698	$BVRI$	2006-01-29	N	2004-04-16	N
NGC 3672	BI	2004-01-20	P	2004-01-17	N
NGC 6810	V	2003-05-28	P	2005-09-04	N
NGC 6861	$BVRI$	2005-09-08	N	2003-05-25	N
NGC 6887	V	2005-05-07	P	2005-09-06	N
NGC 6943	$BVRI$	2005-09-08	N	2005-05-10	N
NGC 7083	$BVRI$	2005-09-08	N	2004-10-14	N
NGC 7329	$BVRI$	2005-09-05	N	2004-10-14	N
NGC 7410	V	2005-09-06	N	2005-09-09	N
NGC 7590	$BVRI$	2005-09-08	N	2004-10-10	N

NOTE.— Col. (1) Galaxy name. Col. (2) Filter. Cols. (3)–(4) Observation date and photometric condition of the images used in the primary sample. Cols. (5)–(6) Observation date and photometric condition of the images used in the comparison sample. In Cols. (4) and (6), "P" means photometric, and "N" means nonphotometric.

Figure 16 compares nine measured parameters derived from the set of repeat observations. Observation 1 denotes the measurement with better quality that has been adopted in the final database of the survey, and Observation 2 gives the comparison measurement. We can see that overall the agreement is quite good. Notable exceptions can be identified with galaxies that have especially unreliable sky values, such as NGC 2434, which is the most deviant outlier in the R_{80} plot (this quantity is sensitive to data at large radii). The average differences and standard deviations of the parameters plotted in Figure 16 are listed in Table 9. The average differences are quite close to 0, and the scatter is small.

TABLE 9: Parameter Differences for the Internal Comparison Sample

	ΔD_{25} ($''$) (1)	$\Delta D_{26.5}$ ($''$) (2)	Δe (3)	ΔPA ($^\circ$) (4)	Δm_{25} (mag) (5)	Δm_{tot} (mag) (6)	ΔR_{20} ($''$) (7)	ΔR_{50} ($''$) (8)	ΔR_{80} ($''$) (9)
Mean	-1.21	-3.86	0.004	5.53	0.01	0.01	0.09	0.25	0.06
Standard deviation	20.42	46.52	0.059	23.39	0.09	0.10	0.81	3.13	11.83

NOTE.— Mean difference and its standard deviation for Col. (1) the isophotal diameter at 25 mag arcsec^{-2}, Col. (2) the isophotal diameter at 26.5 mag arcsec^{-2}, Col. (3) ellipticity, Col. (4) position angle, Col. (5) total apparent magnitude within $\mu = 25$ mag arcsec^{-2}, Col. (6) total apparent magnitude within the last reliable isophote (1 σ above the sky), Col. (7) radius enclosing 20% of the total flux, Col. (8) radius enclosing 50% of the total flux, and Col. (9) radius enclosing 80% of the total flux.
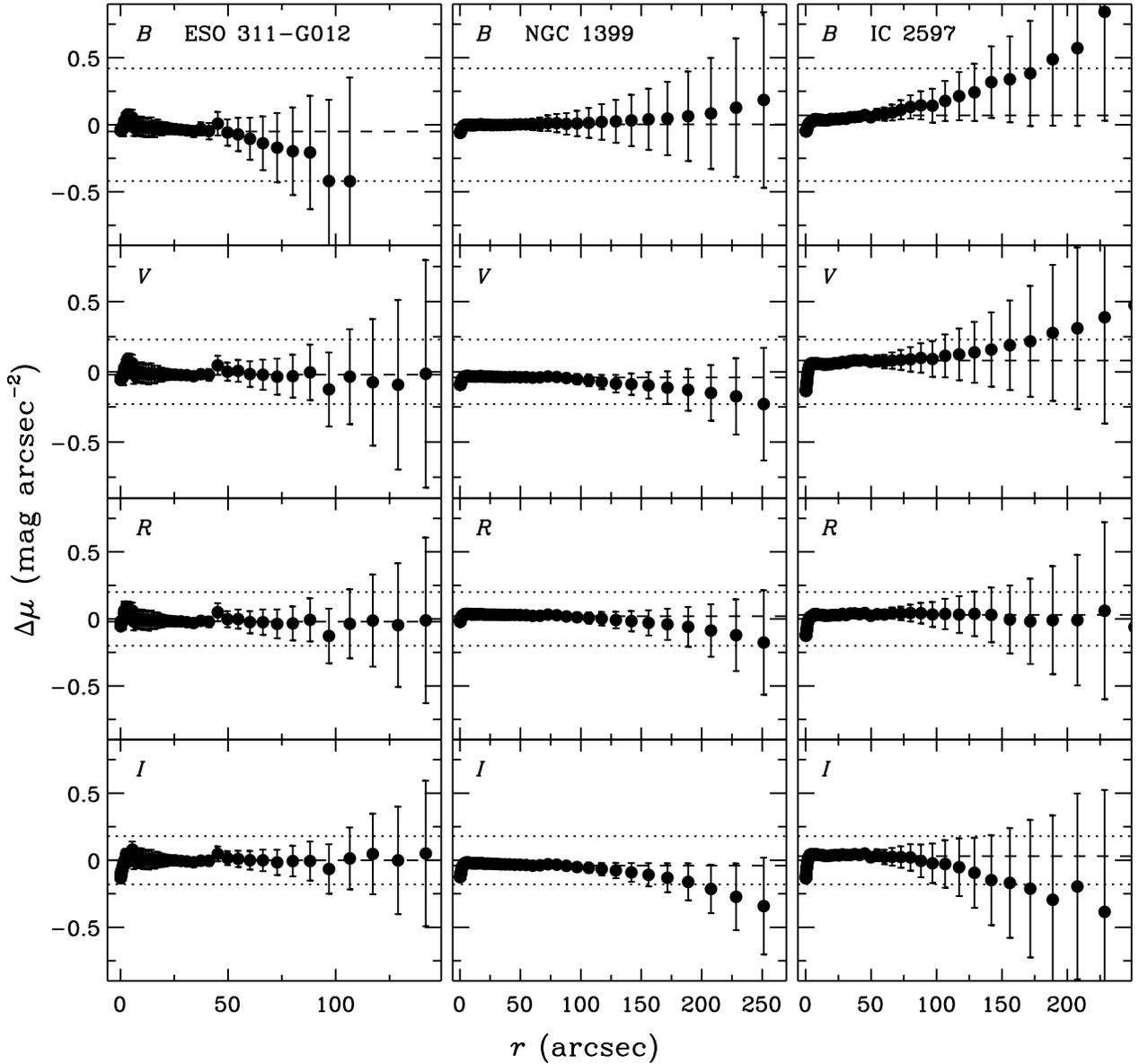
FIG. 15.— Internal comparison of the surface brightness profiles for the objects for which we have repeat observations. The data points are calculated by subtracting one profile from another. The horizontal dashed line in each panel is the weighted average of the residual data, and the two horizontal dotted lines mark the 1 σ photometric uncertainty of the two observations.

10.2. *External Comparison with HyperLeda*

Several of the global parameters measured in our sample have independent data listed in HyperLeda[13] (Paturel et al. 2003), which we can use to perform an external comparison of our errors. Figure 17 compares the following six parameters between CGS and HyperLeda: total I-band magnitude (I_{tot}), total B-band magnitude (B_{tot}), integrated $B-V$ color, isophotal diameter at 25 B mag arcsec^{-2} (D_{25}), e, and PA. The overall agreement is quite good for the integrated magnitudes, $B-V$ color, and D_{25} diameters, especially for the red open points, which represent galaxies that were observed under photometric conditions, that have no contamination from the nearby bright

stars, and that have reliable sky values. The PA comparison improves dramatically after isolating the subset with $e \geq 0.3$. When the galaxy is round, the PA is hard to determine because the semi-major axis for any given isophote is ill-defined. In addition, extreme outliers lying on the lower-right and upper-left corners of the distribution can be attributed to the 180-degree ambiguity for PA's close to 0° or 180°. The ellipticities show by far the worst agreement. The large scatter may be due in part to the fact that the HyperLeda values pertain to measurements made at $\mu_B = 25$ mag arcsec^{-2}, whereas ours are made at a significantly lower surface brightness threshold, at $\mu_B \approx 27$ mag arcsec^{-2}. A more serious problem may be related to inherent biases and errors that are known to plague the axial ra-
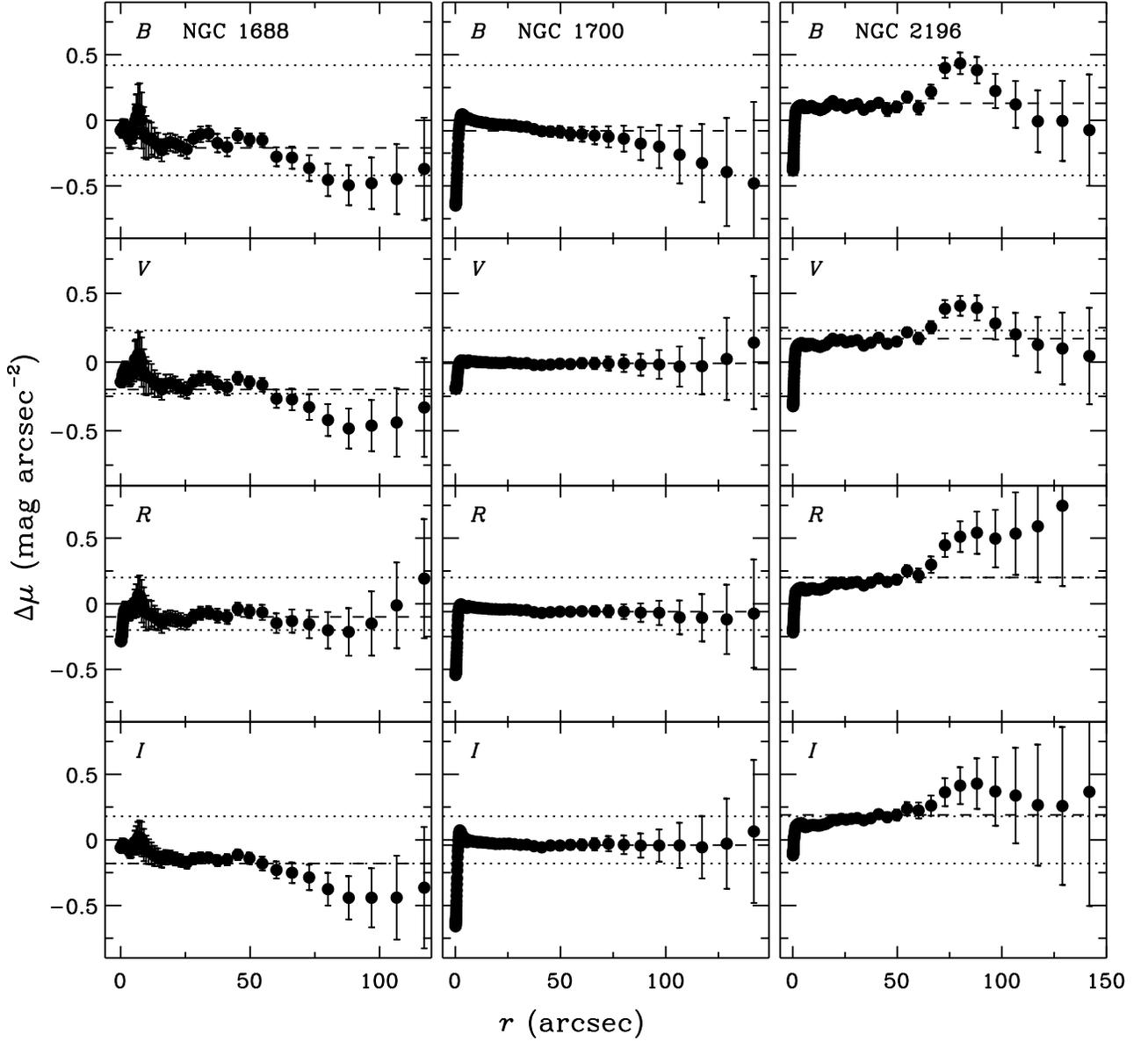
FIG. 15.— continued

tios (ellipticities) contained in the HyperLeda database (see Appendix of Ho 2007).

10.3. *External Comparison with SDSS*

Roughly 9% of the CGS galaxies overlap with the Sloan Digital Sky Survey (SDSS; York et al. 2000; Stoughton et al. 2002), which provides well-calibrated, uniform optical images with a photometric accuracy of 2% − 3%. The SDSS images are available in the *ugriz* filters, but the *u* and *z* images have very low S/N, and we concentrate our attention on the *g, r,* and *i* bands. We analyze the SDSS data following exactly the same procedures applied to the CGS. After registering the *g* and *r* images to the *i* image, we extract isophotal intensity profiles as described in Section 4.1. As the SDSS images were observed in a drift-scan mode, they have both a very large field-of-view and an exceptionally uniform background (Pohlen & Trujillo 2006). This

allows us to determine accurate sky values using the method of Noordermeer & van der Hulst (2007), as described in Section 3. To convert the SDSS *gri* photometry into our standard *BVRI* system, we use the transformation equations given in Jester et al. (2005):

$$B = g + 0.39(g-r) + 0.21 \qquad (9)$$
$$V = g - 0.59(g-r) - 0.01 \qquad (10)$$
$$R = V - 1.09(r-i) - 0.22 \qquad (11)$$
$$I = R - 1.00(r-i) - 0.21. \qquad (12)$$

Figure 18 compares the surface brightness profiles from CGS with those derived from SDSS, for a subset of four relatively small galaxies (NGC 936, 1084, 1087 and 1090) that have well-measured sky values. The profiles are truncated at the radius
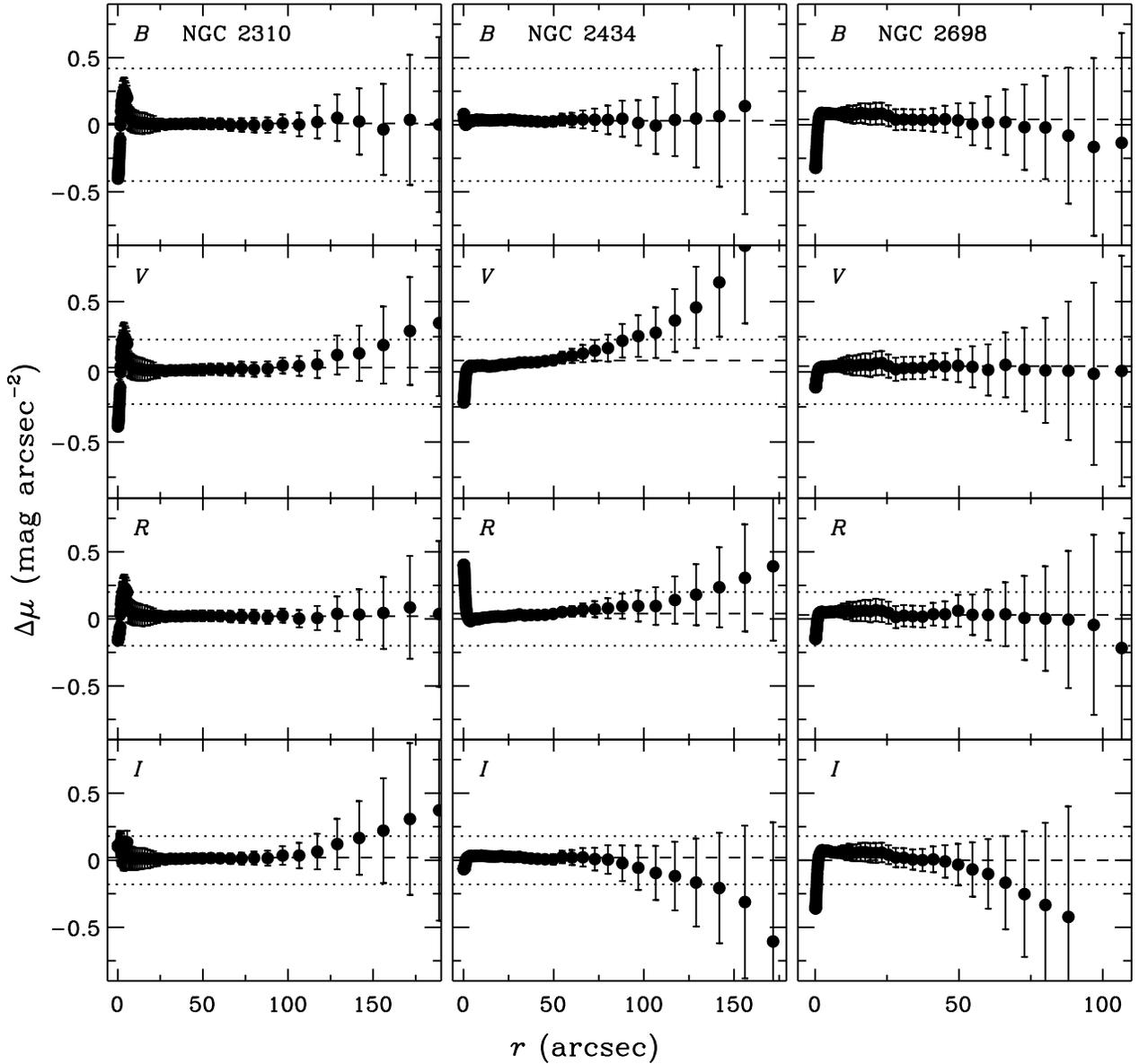
FIG. 15.— continued

where the isophotal intensity is 1σ above the local sky value. It is clear that most of the profiles agree well with each other. The absolute value of the average profile differences are 0.24, 0.14, 0.08, and 0.14 mag arcsec^{-2} for $B, V, R,$ and I band, respectively. This level of discrepancy is not unexpected, given that all four of these galaxies were observed under nonphotometric conditions in CGS, not to mention of additional uncertainties introduced by the photometric transformation from the SDSS to the CGS system. This comparison confirms that the basic reduction and calibration of the CGS data are sound.

Despite the short exposures of the SDSS images (54 s), they have superior background uniformity and better sky determination than CGS. These advantages translate to better sensitivity in terms of surface brightness, by $\sim 0.4, 0.2, 0.6,$ and 0.9 mag arcsec^{-2} in the $B, V, R,$ and I band, respectively. However,

the longer integration times, better seeing, and finer pixel scale of the CGS images imply that they have much higher S/N and sensitivity to compact structures compared to SDSS, typically by a factor of $\sim 4-5$.

11. SUMMARY

We present a comprehensive isophotal analysis of optical ($BVRI$) images for a statistically complete, magnitude-limited sample of 605 bright, southern galaxies, observed as part of the Carnegie-Irvine Galaxy Survey (CGS). We discuss our strategy for determining the sky level and its error. It is challenging to achieve very accurate sky subtraction with our images because the CGS galaxies are relatively large and the background suffers from low-level non-uniformities due to residual flat-fielding errors. Nevertheless, cross-checks with internal and external data indicate that our calibration and sky subtraction
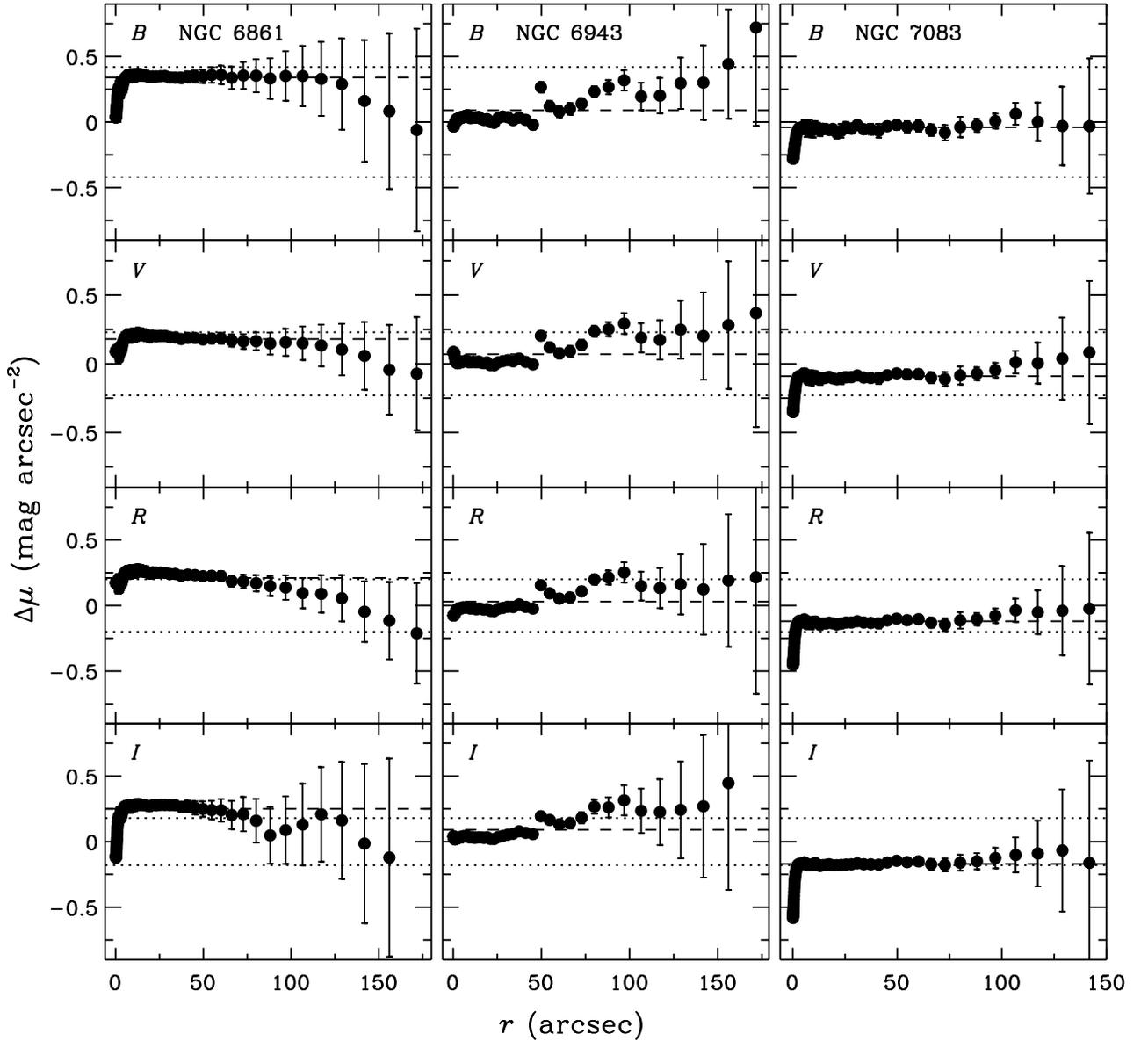
F<small>IG</small>. 15.— continued

strategies are robust, and that our quoted measurement uncertainties are sound.

This paper focuses on the derivation of radial profiles of surface brightness, color, and various geometric parameters that characterize the shape and orientation of the isophotes. We construct composite brightness profiles as a function of Hubble type to highlight statistical trends. Non-exponential disks are seen in many S0 and spiral galaxies. We perform a Fourier analysis of the isophotes to characterize their nonaxisymmetric deviations from pure ellipses. The relative amplitude of the $m = 1$ mode effectively identifies lopsided structures in the light distribution, which we find to be common in our sample, especially among late-type galaxies. Bars and spiral arms, by contrast, are best revealed by the relative amplitude of the $m = 2$ Fourier mode. We present a uniform set of quantitative mea-

surements of bar size and bar strength, spiral arm strength, and lopsidedness amplitudes.

Forthcoming papers will utilize the databases assembled here and in Paper I to explore a number of scientific issues, including

1. Statistics of bars, bar properties, and their possible connection to spiral arms.

2. Incidence of lopsidedness and its dependence on global galaxy and environmental parameters.

3. Disk profiles, truncations, and correlations with color gradients.
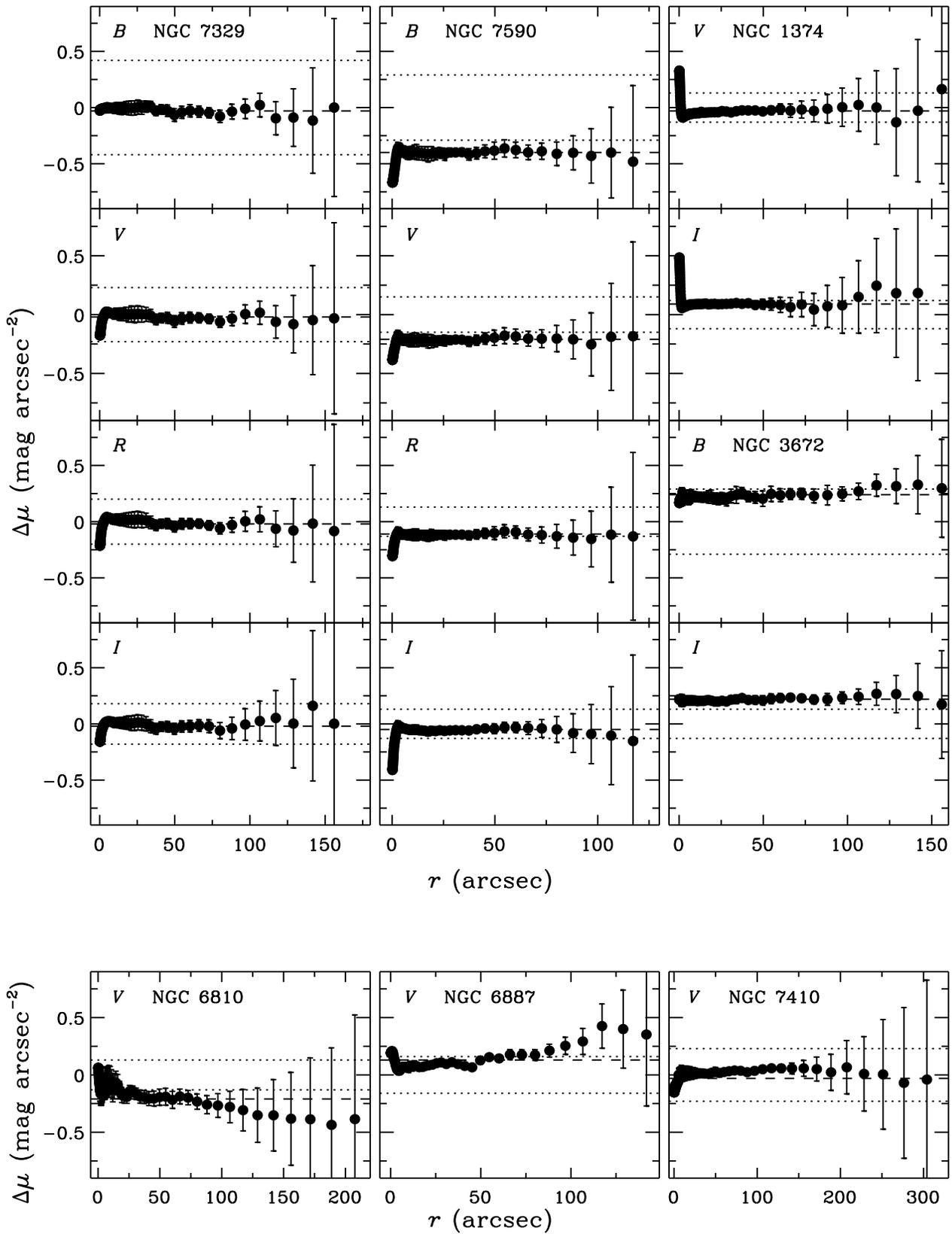
FIG. 15.— continued
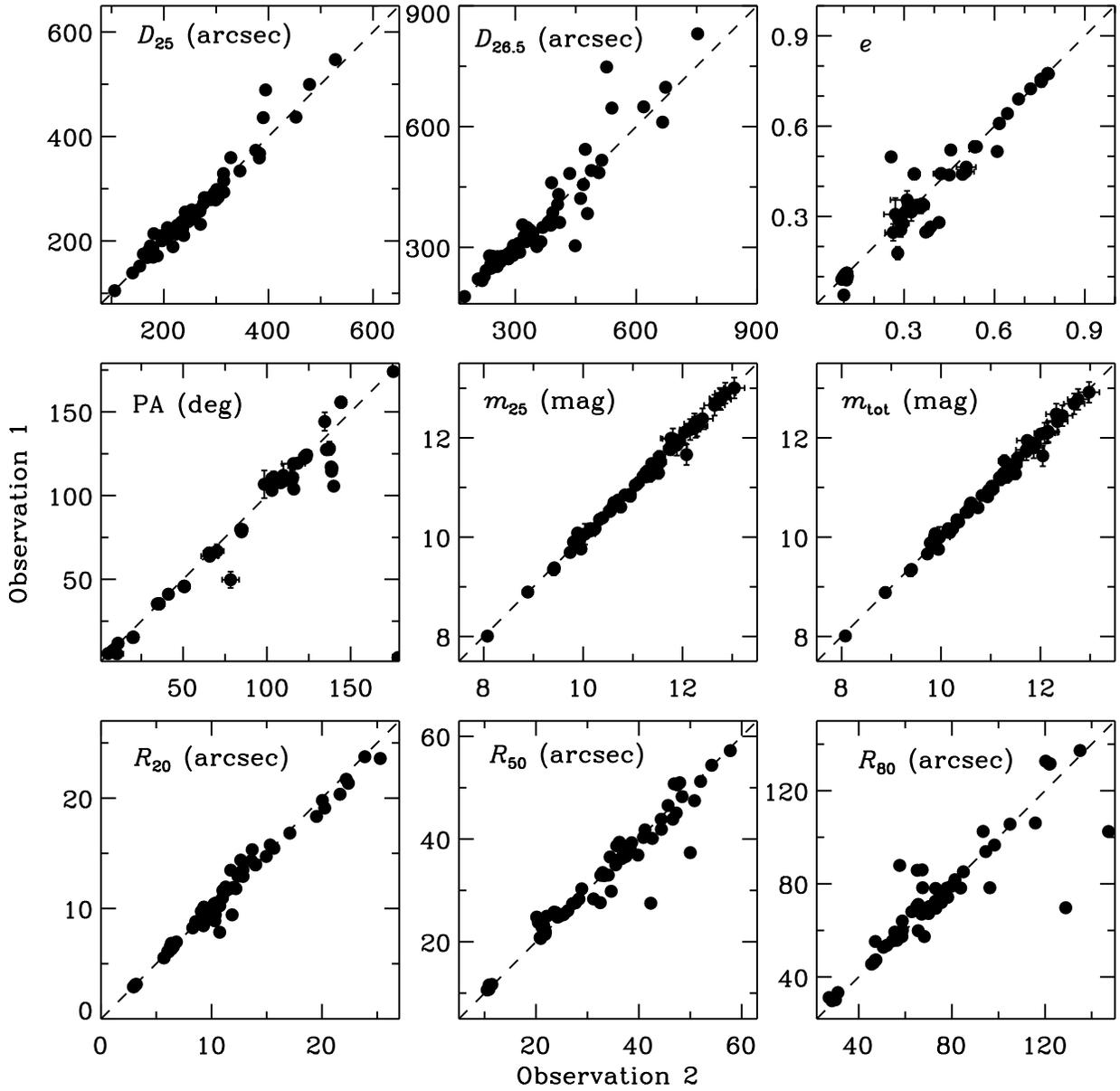
FIG. 16.— Internal comparison of derived parameters for objects with repeat observations. Observation 1 denotes values we adopt in the survey, while Observation 2 gives the reference values for internal comparison. The dashed line denotes $y = x$.

FIG. 17.— External comparison of derived parameters between CGS and HyperLeda. The full sample available for comparison is shown as black squares, while the red open points mark the subset with the smallest measurement uncertainty. For I_{tot}, B_{tot}, $B-V$, and D_{25}, the most reliable points are those that were observed under photometric conditions, that have well-measured sky values, and that do not suffer from contamination by nearby bright field stars. For e the red points highlight objects with minimal bright star contamination, and for the PA we additionally require that $e \geq 0.3$. The dashed line denotes $y = x$.
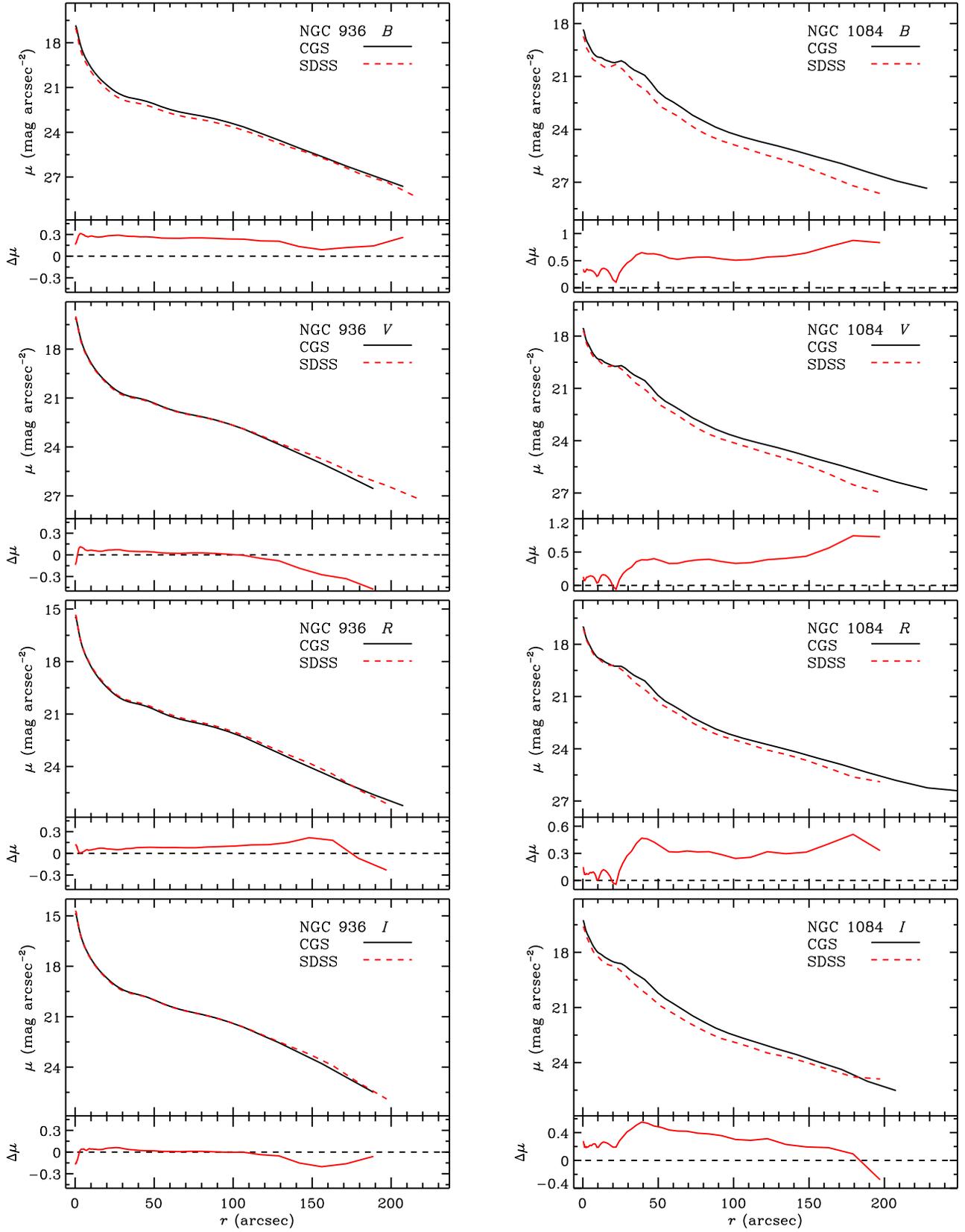
FIG. 18.— Comparison between the surface brightness profiles derived from CGS and SDSS. The SDSS data were analyzed in the same way as the CGS data, and their photometric system was transformed to ours as described in Section 10.3. Within each panel, the upper subpanel shows the two profiles, truncated at the radius where the isophotal intensity is 1 σ above the local sky background; the bottom subpanel shows the difference between the CGS and SDSS profiles.
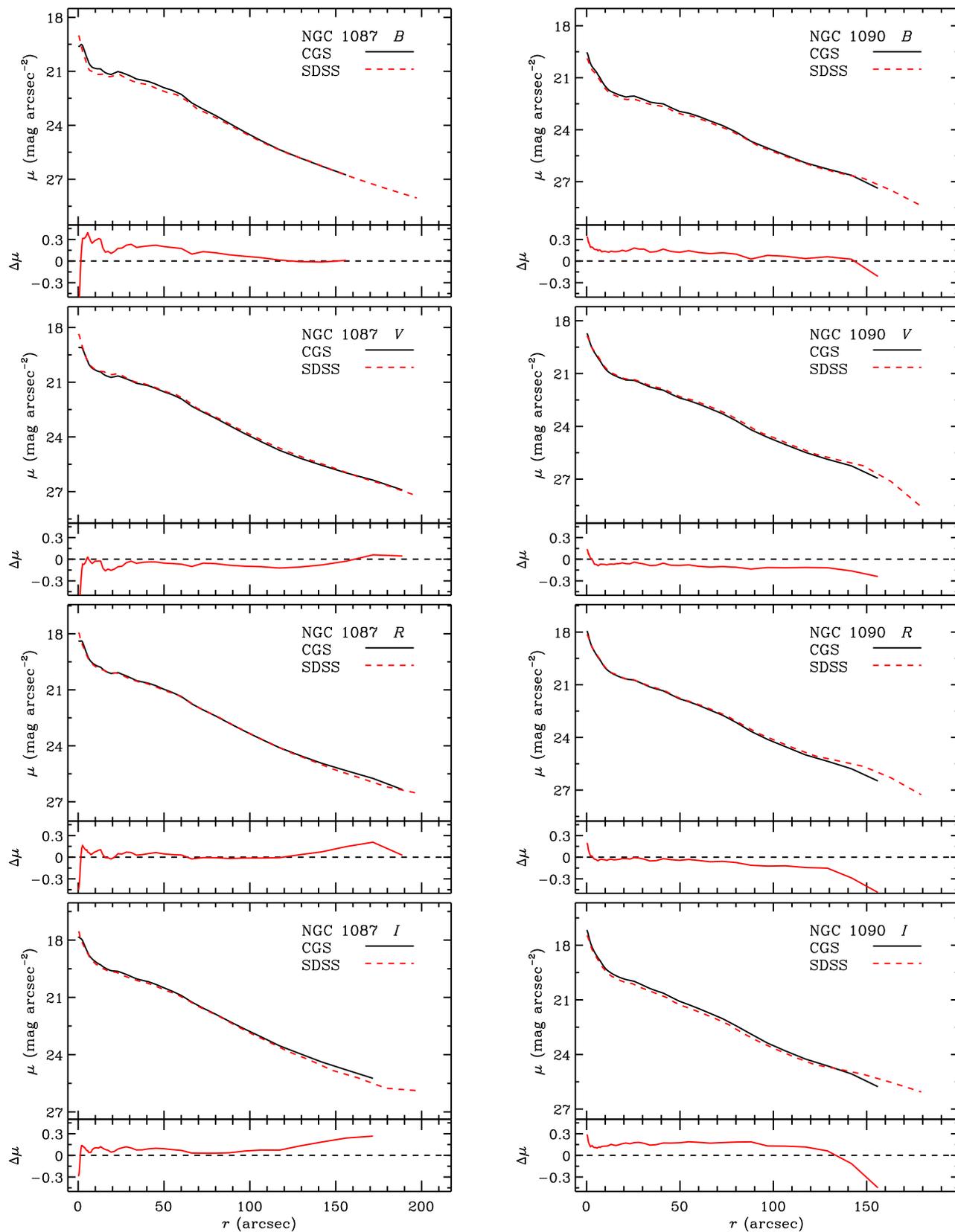
FIG. 18.— continued

REFERENCES

Aguerri, J. A. L., Debattista, V. P., & Corsini, E. M. 2003, MNRAS, 338, 465
Aguerri, J. A. L., Elias-Rosa, N., Corsini, E. M., & Muñoz-Tuñón, C. 2005, A&A, 434, 109
Aguerri, J. A. L., Méndez-Abreu, J., & Corsini, E. M. 2009, A&A, 495, 491
Andredakis, Y. C., Peletier, R. F., & Balcells, M. 1995, MNRAS, 275, 874
Andredakis, Y. C., & Sanders, R. H. 1994, MNRAS, 267, 283
Athanassoula, E., & Misiriotis, A. 2002, MNRAS, 330, 35
Barazza, F. D., Jogee, S., & Marinova, I. 2008, ApJ, 675, 1194
Bournaud, F., Combes, F., Jog, C. J., & Puerari, I. 2005, A&A, 438, 507
Buta, R. 1986, ApJS, 61, 631
Buta, R., & Block, D. L. 2001, ApJ, 550, 243
Caon, N., Capaccioli, M., & D'Onofrio, M. 1993, MNRAS, 265, 1013
Carter, D. 1978, MNRAS, 182, 797
Courteau, S., de Jong, R. S., & Broeils, A. H. 1996, ApJ, 457, 73
de Grijs, R. 1998, MNRAS, 299, 595
de Grijs, R., Kregel, M., & Wesson, K. H. 2001, MNRAS, 324, 1074
de Jong, R. S. 1996, A&AS, 118, 557
de Vaucouleurs, G. 1948, Ann. Astrophys, 11, 247
de Vaucouleurs, G. 1959, in Handbuch der Physik, Bd. LIII, ed. S. Flugge(Berlin: Springer-Verlag), 275
de Vaucouleurs, G., de Vaucouleurs, A., Corwin, H. G., Buta, R. J., Paturel, G., & Fouqué, P. 1991, Third Reference Catalogue of Bright Galaxies (New York: Springer-Verlag)
D'Onofrio, M., Capaccioli, M., & Caon, N. 1994, MNRAS, 271, 523
Elmegreen, B. G., & Elmegreen, D. M. 1985, ApJ, 288, 438
Elmegreen, B. G., Seiden, P. E., & Elmegreen, D. M. 1989, ApJ, 343, 602
Erwin, P. 2005, MNRAS, 364, 283
Erwin, P., Beckman, J. E., & Pohlen, M. 2005, ApJ, 626, 81
Erwin, P., Pohlen, M., & Beckman, J. E. 2008, AJ, 135, 20
Ferguson, A. M. N., & Clarke, C. J. 2001, MNRAS, 325, 781
Ferrarese, L., et al. 2006, ApJS, 164, 334
Fisher, D. B., & Drory, N. 2008, AJ, 136, 773
Freeman, K. C. 1970, ApJ, 160, 811
Fry, A. M., Morrison, H. L., Harding, P., & Boroson, T. A. 1999, AJ, 118, 1209
Gadotti, D. A. 2008, MNRAS, 384, 420
Gadotti, D. A., Athanassoula, E., Carrasco, L., Bosma, A., de Souza, R. E., & Recillas, E. 2007, MNRAS, 381, 943
Governato, F., Willman, B., Mayer, L., Brooks, A., Stinson, G., Valenzuela, O., Wadsley, J., & Quinn, T. 2007, MNRAS, 374, 1479
Graham, A. W. 2001, AJ, 121, 820
Graham, A., & Colless, M. 1997, MNRAS, 287, 221
Graham, A., Lauer, T. R., Colless, M., & Postman, M. 1996, ApJ, 465, 534
Gunn, J. E., et al. 1998, AJ, 116, 3040
Ho, L. C. 2007, ApJ, 668, 94
Ho, L. C., Li, Z.-Y., Barth, A. J., Seigar, M., & Peng, C. Y. 2011, ApJS, submitted (Paper I)
Hubble, E. 1926, ApJ, 64, 321
Jedrzejewski R. I. 1987, MNRAS, 226, 747
Jester, S., et al. 2005, AJ, 130, 873
Jog, C. J., & Combes, F. 2009, Phys. Rep., 471, 75
Jogee, S., et al. 2004, ApJ, 615, 105
Katz, N. 1991, ApJ, 368, 325
King, I. R. 1978, ApJ, 222, 1
Kormendy, J. 1979, ApJ, 227, 714
Kormendy, J., & Djorgovski, S. 1989, ARA&A, 27, 235
Kormendy, J., Fisher, D. B., Cornell, M. E., & Bender, R. 2009, ApJS, 182, 216
Kormendy, J., & Kennicutt, R. C. 2004, ARA&A, 42, 603

Laine, S., Shlosman, I., Knapen, J. H., & Peletier, R. F. 2002, ApJ, 567, 97
Lauer, T. R., et al 1995, AJ, 110, 2622
Laurikainen, E., Salo, H., & Buta, R. 2005, MNRAS, 362, 1319
MacArthur, L. A., Courteau, S., & Holtzman, J. A. 2003, ApJ, 582, 689
Marinova, I., & Jogee, S. 2007, ApJ, 659, 1176
Martin, P. 1995, AJ, 109, 2428
Martinet, L., & Friedli, D. 1997, A&A, 323, 363
Matthews, L. D., & Gallagher III, J. S. 1997, AJ, 114, 1899
Menéndez-Delmestre, K., Sheth, K., Schinnerer, E., Jarrett, T. H., & Scoville, N. Z. 2007, ApJ, 657, 790
Milvang-Jensen, B., & Jørgensen, I. 1999, Baltic Astron., 8, 535
Noordermeer, E., & van der Hulst, J. M. 2007, MNRAS, 376, 1480
Odewahn, S. C., Cohen, S. H., Windhorst, R. A., & Philip, N. S. 2002, ApJ, 568, 539
Ohta, K., Hamabe, M., & Wakamatsu, K. 1990, ApJ, 357, 71
Paturel G., Petit C., Prugniel P., Theureau G., Rousseau J., Brouty M., Dubois P., & Cambrésy L. 2003, A&A, 412, 45
Peletier, R. F., Davies, R. L., Illingworth, G. D., Davis, L. E., & Cawson, M. 1990, AJ, 100, 1091
Peng, C. Y., Ho, L. C., Impey, C. D., & Rix, H.-W. 2010, AJ, 139, 2097
Phillipps, S., Evans, R., Davies, J. I., & Disney, M. J. 1991, MNRAS, 253, 496
Pohlen, M., Dettmar, R.-J., & Lütticke, R. 2000, A&A, 357, L1
Pohlen, M., Dettmar, R.-J., Lütticke, R., & Aronica, G. 2002, A&A, 392, 807
Pohlen, M., & Trujillo, I. 2006, A&A, 454, 759
Prieto, M., Gottesman, S. T., Aguerri, J. A. L., & Varela, A. M. 1997, AJ, 114, 1413
Reichard, T. A., Heckman, T. M., Rudnick, G., Brinchmann, J., Kauffmann, G., & Wild, V. 2008, ApJ, 677, 186
Rix, H.-W., & Zaritsky, D. 1995, ApJ, 447, 82
Robertson, B., Yoshida, N., Springel, V., & Hernquist, L. 2004, ApJ, 606, 32
Sandage, A. 1961, The Hubble Atlas of Galaxies (Washington, DC: Carnegie Inst. Washington)
Schlegel, D. J., Finkbeiner, D. P., & Davis, M. 1998, ApJ, 500, 525
Schombert, J. M. 1986, ApJS, 60, 603
Sérsic, J. L. 1968, Atlas de Galaxias Australes (Córdoba: Obs. Astron., Univ. Nac. Córdoba)
Silva, D. R., & Elston, R. 1994, ApJ, 428, 511
Slyz, A. D., Devriendt, J. E. G., Silk, J., & Burkert, A. 2002, MNRAS, 333, 894
Stoughton, C., et al. 2002, AJ, 123, 485
Taylor, V. A., Jansen, R. A., Windhorst, R. A., Odewahn, S. C., & Hibbard, J. E. 2005, ApJ, 630, 784
Trujillo, I., Graham, A. W., & Caon, N. 2001, MNRAS, 326, 869
Trujillo, I., Ramos, A. A., Rubiño-Martín, J. A., Graham, A. W., Aguerri, J. A. L., Cepa, J., & Gutiérrez, C. M. 2002, MNRAS, 333, 510
van Albada, T. S. 1982, MNRAS, 201, 939
van der Kruit, P. C. 1979, A&AS, 38, 15
van der Kruit, P. C., & Freeman, K. C. 2011, ARA&A, in press (arXiv:1101.1771)
van der Kruit, P. C., & Searle, L. 1981, A&A, 95, 116
van Eymeren, J., Juette, E., Jog, C. J., Stein, Y., & Dettmar, R.-J. 2011, A&A, in press (arXiv:1103.4929)
Wu H., et al. 2002, AJ, 123, 1364
York, D. G., et al. 2000, AJ, 120, 1579
Yoshii, Y., & Sommer-Larsen, J. 1989, MNRAS, 236, 779
Zaritsky, D., & Rix, H.-W. 1997, ApJ, 477, 118
Zhang, B., & Wyse, R. F. G. 2000, MNRAS, 313, 310

APPENDIX

DATABASE OF ISOPHOTAL PARAMETERS

Figures A1–A616 present the database of isophotal parameters for the 605 galaxies in CGS; we also include the 11 extra galaxies that are not part of the formal sample. One full-page figure is devoted to each galaxy, ordered sequentially following the numerical indices listed in Column (1) of Table 2. In the lower-left panel, we give the B, V, R, and I surface brightness profiles, followed by the $B-I$, $V-I$, and $R-I$ color profiles. The lower-right panel shows the radial profiles of e, PA, A_3 (blue triangles) and B_3 (red circles), A_4 (blue triangles) and B_4 (red circles), I_1/I_0 (black triangles) and ϕ_1 (red circles), and I_2/I_0 (black triangles) and ϕ_2 (red circles). The horizontal dashed lines in the e and PA subpanels denote the characteristic values of the galaxy. The top two panels show the BVI color composite image, displayed using an arcsinh stretch, and the star-cleaned I-band structure map, displayed using a linear stretch. These are helpful to show side-by-side with the isophotal plots to aid in the identification and interpretation of specific features in the 1-D radial profiles. We only display three sample pages for illustration; the full set of figures is available in the electronic version of the paper, as well as on the project website http://cgs.obs.carnegiescience.edu.
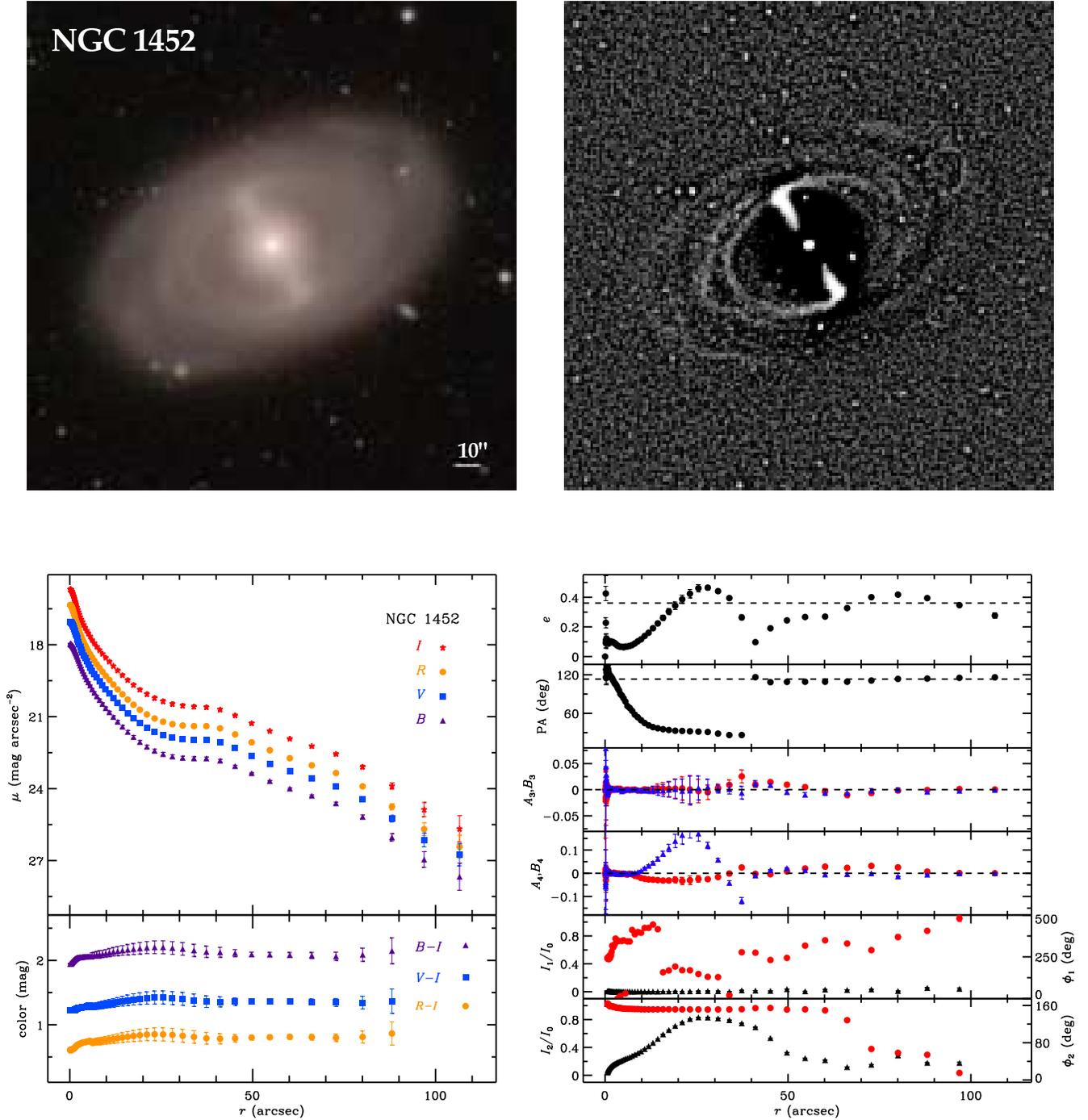
FIG. A222.— Brightness profiles and isophotal parameters for the barred SB0/a galaxy NGC 1452. The color composite image is shown on the upper left, displayed using an arcsinh stretch, and the star-cleaned I-band structure map is shown on the upper right, displayed using a linear stretch. The lower-left panel gives the B, V, R, and I surface brightness profiles, followed by the $B-I$, $V-I$, and $R-I$ color profiles. The lower-right panel shows the radial profiles of e, PA, A_3 (blue triangles) and B_3 (red circles), A_4 (blue triangles) and B_4 (red circles), I_1/I_0 (black triangles) and ϕ_1 (red circles), and I_2/I_0 (black triangles) and ϕ_2 (red circles). The horizontal dashed lines in the e and PA subpanels denote the characteristic values of the galaxy.

FIG. A361.— Brightness profiles and isophotal parameters for the lopsided SBc galaxy NGC 3513. The color composite image is shown on the upper left, displayed using an arcsinh stretch, and the star-cleaned I-band structure map is shown on the upper right, displayed using a linear stretch. The lower-left panel gives the B, V, R, and I surface brightness profiles, followed by the $B-I$, $V-I$, and $R-I$ color profiles. The lower-right panel shows the radial profiles of e, PA, A_3 (blue triangles) and B_3 (red circles), A_4 (blue triangles) and B_4 (red circles), I_1/I_0 (black triangles) and ϕ_1 (red circles), and I_2/I_0 (black triangles) and ϕ_2 (red circles). The horizontal dashed lines in the e and PA subpanels denote the characteristic values of the galaxy.

FIG. A583.— Brightness profiles and isophotal parameters for the barred SBb galaxy NGC 7329. The color composite image is shown on the upper left, displayed using an arcsinh stretch, and the star-cleaned I-band structure map is shown on the upper right, displayed using a linear stretch. The lower-left panel gives the B, V, R, and I surface brightness profiles, followed by the $B-I$, $V-I$, and $R-I$ color profiles. The lower-right panel shows the radial profiles of e, PA, A_3 (blue triangles) and B_3 (red circles), A_4 (blue triangles) and B_4 (red circles), I_1/I_0 (black triangles) and ϕ_1 (red circles), and I_2/I_0 (black triangles) and ϕ_2 (red circles). The horizontal dashed lines in the e and PA subpanels denote the characteristic values of the galaxy.